Title

Enabling fast charging of lithium-ion batteries through secondary- /dual- pore network: Part I - Analytical diffusion model

Authors

Usseglio-Viretta, FLE
Mai, W
Colclasure, AM
et al.

Publication Date

2020-05-01

DOI

10.1016/j.electacta.2020.136034

Peer reviewed

Journal Pre-proof

Enabling fast charging of lithium-ion batteries through secondary- /dual- pore network: Part I - Analytical diffusion model

F.L.E. Usseglio-Viretta, W. Mai, A.M. Colclasure, M. Doeff, Eongyu Yi, K. Smith

PII: S0013-4686(20)30426-6

DOI: https://doi.org/10.1016/j.electacta.2020.136034

Reference: EA 136034

To appear in: *Electrochimica Acta*

Received Date: 6 December 2019

Revised Date: 5 March 2020

Accepted Date: 6 March 2020

Please cite this article as: F.L.E. Usseglio-Viretta, W. Mai, A.M. Colclasure, M. Doeff, E. Yi, K. Smith, Enabling fast charging of lithium-ion batteries through secondary- /dual- pore network: Part I - Analytical diffusion model, *Electrochimica Acta* (2020), doi: https://doi.org/10.1016/j.electacta.2020.136034.

Enabling Fast Charging of Lithium-Ion Batteries through Secondary- /Dual- Pore Network: Part I - Analytical Diffusion Model

F. L. E. Usseglio-Viretta[1], W. Mai[1], A. M. Colclasure[1], M. Doeff[2], Eongyu Yi[2], and K. Smith[1]

[1] Center for Integrated Mobility Sciences, National Renewable Energy Laboratory, Golden, CO 80401 USA

[2] Energy Storage and Distributed Resources Division, Lawrence Berkeley National Laboratory, Berkeley, CA 94720 USA

Corresponding author: A. Colclasure. Email address: Andrew.Colclasure@nrel.gov

Abstract

Battery performance is strongly correlated with electrode microstructural properties. Enabling fast charging of lithium-ion batteries requires improved through-plane ionic diffusion that can be achieved through, among other strategies, structured electrodes with a secondary- or dual-pore network (SPN). In this work, an analytical model investigates the impact of such an SPN on ionic diffusion with a composite electrode, considering various pore-channel geometries and comparing to standard electrodes with identical gravimetric- and volumetric-specific theoretical capacities. Relevant SPN design parameters and tortuosity coefficients are identified according to three optimization objectives that aim to balance the improved overall through-plane diffusion, thanks to the coarse aligned channels, and degraded in-plane diffusion because of the porous matrix densification required to maintain gravimetric- and volumetric-specific theoretical capacities. The model indicates that a relatively low amount of SPN is required and that electrodes with high through-plane tortuosity and low in-plane tortuosity benefit most from such architecture.

Keywords: secondary-pore network, dual-pore network, lithium-ion battery, laser ablation, freeze-casting

1. Introduction

Fast ion transport along the cell thickness is required for lithium-ion batteries (LIB) to sustain continuous high-rate discharge or charge currents, which is a desired feature for the fast charging of electric vehicle batteries [1,2,3,4]. LIB electrodes have complex porous microstructures, which are linked to the macroscopic performance of these devices. Specifically, the effective, or macroscopic, ionic diffusion coefficient D_{eff} is related to the porosity ε and the tortuosity factor τ (cf. eq. 1). The latter denotes the effect of the convoluted, tortuous path of the pores that hinders the lithium-ion diffusion and is often correlated with the porosity according to the generalized Archie's relationship (cf. eq. 2), which is an empirical generalization of the Bruggeman analytical law [5,6]. The bulk (i.e., dense) diffusion coefficient is noted D_0, the normalized effective diffusion coefficient is noted D_n, and the two fitted coefficients of the Archie's relationships are noted γ and α. Previous work demonstrated that tortuosity factor is a key parameter to enable fast charge for thick electrodes without capacity loss induced by either lithium plating in the anode and/or electrode-active material partial utilization due to local electrolyte depletion [1]. It is then relevant for automotive applications to design LIB electrodes with the lowest possible through-plane (i.e., along the electrode thickness) tortuosity factor.

$$D_n = \frac{D_{eff}}{D_0} = \frac{\varepsilon}{\tau} \quad [1]$$

$$\tau = \gamma \varepsilon^{1-\alpha} \quad [2]$$

Advances in LIB electrode manufacturing have, to a certain extent, enabled control of the electrode microstructure architecture. For example, several groups [7–20] have experimentally tested architectures tailored specifically to increase the through-plane ionic diffusion for fast charge application by adding channels or groove-like large pores oriented along the electrode thickness (cf. Fig. 1). These voids do not replace the existing pores of the electrode microstructure but consist in a second, coarser pore network. The concept is that lithium ions will first preferentially diffuse through these straight large channels (i.e., through the path of least resistance) between the current collector and the separator, and then in-plane through the fine pore network to reach the reaction site. For the remainder of this article, such architectured microstructures are referred to as the secondary- or dual-pore network (SPN).

In this work, we investigate, through modeling, the impact of SPN on diffusion, LIB electrochemical performances and degradation, to eventually provide SPN design recommendations for fast-charge applications. For clarity, this work is divided into two articles. Part I (present article) provides a comprehensive review of the different techniques available to manufacture such advanced architectures (cf. §2). The impact of an SPN on ionic diffusion is modeled through a simple analytical approach introduced in §3.1. Comparisons with baseline electrodes are explained in §3.2. SPN design parameters optimization is considered according to three different diffusion optimization objectives defined in §3.3, and SPN design parameters are introduced in §3.4. Results obtained with the analytical model for two different graphite electrode materials are presented in §4.1. SPN design parameters sensitivity with transport coefficients is investigated in §4.2. A macro-homogeneous pseudo-two-dimensional (2D) model from a previous work [1] is used in §5 to initially investigate the SPN impact on cell performances during fast charge considering both typical (non-architectured electrode) and low

(architectured electrode) tortuosity factor values. Part II [21] refines the analysis relying on a 2D electrochemical model that explicitly takes into consideration the in-plane transport, which is a key aspect of an SPN. In this frame, the simpler-but-faster analytical diffusion model must be considered as a prescreening tool to quickly investigate a large design space. Conversely, the numerical electrochemical model, which is more precise but more computationally expensive, is used to refine the analysis on selected regions of the design space. Additionally, the impact of an SPN on lithium plating degradation mechanisms is investigated in Part II [21]. The two model recommendations are compared at the end of Part II [21]. An advantage to such an approach is to deconvolute the weight of ionic transport from the more complex LIB physics, which is a combination of transport and kinetics processes, on the SPN design recommendation. In other words, can SPN optimal design parameters be deduced, or at least approximated, from a simple diffusion-only analysis, considering ionic transport limitation is the initial reason that led to SPN architectures in the first place? The aim of this two-part work is to identify the design and operation condition domain for which using an SPN provides enough capacity improvement to justify increased manufacturing cost.

2. Review of SPN architectures

Several authors [7–20, 22–25] have proposed different electrode architectures to reduce the tortuosity factor and improve electrochemical cell performance through experiments and modeling. These methods are listed in Table 1 and are detailed below.

Magnetic particle alignment. A first approach consists of taking advantage of the active material anisotropy, if any. Billaud et al. [22] have demonstrated at the laboratory scale a nearly 4 times reduction of the through-plane tortuosity factor for a thick graphite anode via magnetic alignment of the flake-like, anisotropic, graphite particles. This is achieved by coating the non-magnetic particles with superparamagnetic sacrificial nanoparticles (iron oxide) to make the active material magnetically responsive, even with a small magnetic field of 100 mT [22]. As a result, the authors experimentally measured a storage capacity up to 3 times higher at relatively high C-rate compared to the non-aligned electrode [22]. Very similar capacities have been measured at low C-rate (C/10) because ionic transport is not limiting under this regime. Focused ion beam-tomography images of the un-aligned and aligned graphite did not reveal any intrinsic microstructure change except from the overall rotation of the structure. This is corroborated by the substitution of the in-plane tortuosity factor with the through-plane tortuosity factor calculated by the authors after the alignment, which indicated axes have been interchanged [22]. Such a technique is then particularly suited for highly anisotropic materials but is not relevant for isotropic materials. While the authors claim the technique used is scalable and inexpensive, to the authors' knowledge, it has been demonstrated only at the lab scale. The long-term stability of the iron-oxide nanoparticles is also to be assessed. Lastly, the tortuosity factor after alignment was still relatively high, $\tau = 3.8$ at $\varepsilon = 0.32$ (supplementary information of [22]) compared with what can be achieved with spherical particles [1,6,26,27]. This could be explained by the iron-oxide forming aggregates [22] possibly hindering lithium-ion diffusion or by a still-convoluted pathway because of the complex particle morphology, even when aligned.

Magnetic templating. Sander et al. [7] have improved transport properties of $LiCoO_2$ electrodes by magnetically aligned sacrificial emulsion droplets of a ferrofluid or sacrificial nylon microrods coated with superparamagnetic iron-oxide nanoparticles. In both approaches, the sacrificial phase is removed (pyrolysis for the microrods, evaporation for the droplets) after alignment [7]. For both sacrificial phases, scanning electron microscopy (SEM) cross-section images of the microstructures revealed a dual-pore network, with aligned pore channels, with a larger characteristic size compared to the pore microstructure. It then differs from the magnetic particle alignment technique [22] because the microstructure is intrinsically modified. The authors reported the pore-channel spacing had an impact on the capacity at rates higher than 1C, implying it is a key design parameter [7]. For example, the ratio of architectured/non-architectured areal capacities is about a factor of 3 at 2C for a 310-µm thick $LiCoO_2$ electrode with the same total porosity and a pore-channel spacing of 28 µm, while similar capacities are achieved if the spacing is set to 32 µm [7]. For very low C-rate (C/20), both architectured and non-architectured electrodes with the same total porosity share the same areal capacity [7]. Drive-cycle testing reveals aligned-porosity electrodes deliver more than twice the capacity of the baseline electrode before reaching the cutoff voltage, with a 93% capacity retention after 38 cycles [7], demonstrating the efficacy of such architectured electrodes for automotive applications.

Co-extrusion. Bae et al. [8] have calculated the effective electrode tortuosity based on electrolyte concentration drop across the electrode during discharge under a steady-state assumption, considering cylindrical channels. The authors show that the channel-volume ratio as well as the channel-spacing distance normalized over the electrode thickness control the net tortuosity. They have then employed iterative co-extrusion and sintering to fabricate $LiCoO_2$ electrodes with a dual-scale porosity distribution for which they reported higher discharge capacities (up to three times) at the higher C-rate and smaller channel dimension and spacing investigated when compared to baseline electrodes with the same overall porosity. Cobb and Blanco [23] and then Cobb and Solberg [24] have investigated with a macro-homogenous porous electrode 2D model rectangular (groove-like) channel geometries manufacturable with co-extrusion. The authors calculate that the volumetric capacity reaches an asymptote, or a maximum, once the width of the porous matrix gets larger than 3 to 5 times the width of the rectangular channels for very thick $LiCoO_2$ electrodes at 1C discharge rate, indicating that an SPN volume ratio of around 17%–25% is desirable [23]. Ultra-thick co-extruded electrodes (300–400 µm) improve upon the active material utilization ($mAh.g^{-1}$) of their ultra-thick monolithic counterparts by 1.5–5 times [23]. The authors calculate that the current density is higher at the edges of the electrode than in the center, indicating SPN architectures induce higher current density heterogeneity that may eventually trigger earlier degradation even though such density concentrations can be partially relieved by rounding the grooves edges [23]. Cobb and Solberg [24] calculate that keeping a small pad or layer of functional cathode material at the base of the current collector side without an SPN can increase both gravimetric and volumetric energy. Nemani et al. [25] have incorporated the electrode transport anisotropy into a full-cell model. Indeed, non-spherical particles, such as flake-like graphite, exhibit anisotropic tortuosity factors [26,27] and must be considered to properly evaluate the impact of an SPN on the electrochemical performances. In general, the authors found that the effectiveness of SPN decreases as the channel-spacing-to-thickness ratio increases at a constant total porosity [25]. Also, the discharge capacity increases with channel-pore volume ratio as ionic through-plane diffusion is

improving until it reaches a maximum around 15%–25% SPN volume ratio and then decreases [25]. Furthermore, the discharge capacity was improved when both electrodes were structured with grooves.

Laser ablation. Rakebrandt et al. [9] have employed ultra-fast laser ablation to create rectangular channels within thick nickel manganese cobalt oxide (NMC) electrodes without damaging the aluminum substrate or melting the material outside of the laser-structured area. They have demonstrated an increase of the discharge capacity from ~50% to 65% for a 100-µm-thick NMC532 electrode at a 2C discharge rate. In addition, similar cycling capacity retention for the unstructured and laser-structured microstructure have been achieved for the first 10 cycles. Similarly, Park et al. [10] have laser-structured an NMC cathode with uniformly spaced micro-grooves with no evidence of melting at the edge of laser-structured features as well. Because laser processing induces a loss of active material, areal specific capacity measured at 0.1C is higher for the non-structured electrode. However, higher areal specific capacities have been reported for the laser-structured electrodes at higher current rates, especially for the thick and low-porosity electrodes. For example, the normalized discharge capacity was measured at~87% and 72% for architectured and non-architectured electrodes, respectively, at 1C (and ~50% and ~12% at 2C) for a 26% porous and 100-µm thick NMC laser-ablated electrode [10]. Habedank et al. [11] have compared, experimentally and numerically, unstructured and laser-structured graphite anodes in a full cell using a standard unstructured NMC cathode and 64-µm thick electrodes. Electrodes had different theoretical capacities because of the loss of active material induced by laser-structuring in the anode. Discharge areal capacities were improved in the 1C–10C range with the most improvement found in the range of 1C–3C. For example, normalized capacity at 3C charge is 60% and 70%–75%, respectively, for the unstructured anode and the structured anode, with fair agreement between modeling and experiment. Modeling results reveal through-plane concentration gradients were reduced with the structured electrodes. At higher C-rate (>4C), transport within the unstructured cathode became the limiting factor. After 1000 cycles at 1C charging and discharging rate, normalized capacity retention measured on several cells was, on average, ~75% for the unstructured electrodes and ~ 85% for the structured electrodes, with a higher dispersion for the unstructured cells. Unlike [9,10], the SPN geometry here were cylindrical channels. The authors reported the SPN structure is heterogeneous through the electrode surface because it depends on the size and morphology of the laser-structured particles, resulting in different holes [11]. Such heterogeneity has not been reported for groove-like laser processing [9,10].

Microstructure mechanical milling. Cast electrodes are structured with linear macropore cut using flat micro-mill. This technique has been employed for water desalination through capacitive deionization [19,20]. In capacitive deionization, anions and cations are removed from feedwater solution by way of capacitive adsorption into electric double-layers [19]. Achieving high salt removal rates in thick electrodes is critical to making this technique economically feasible. This requires high ionic transport [19]. Reale et al. [19] have manufactured activated carbon electrodes with 100 µm width macroscopic pores along most of the electrode thickness with a trench depth precision of 25 µm. While lower areal capacitance were measured for the structured electrode compared with the unstructured one at low sweep rate (due to its smaller electrode mass), higher values (+115%) were reported for the highest sweep rate and thickest electrode thanks to the low tortuosity of the structured electrode which reduces electrode resistance and enables sustained capacitance at high sweep rates [19].

Freeze-casting (ice-templating). This technique consists of freezing a slurry under controlled conditions so that ice crystals grow in a unidirectional fashion. Solid particles are excluded by the moving ice front during the solidification process and form self-supporting structures trapped between the ice lamellae. The frozen solvent (usually water, but certain organic solvents can also be used) is then removed by sublimation. An optional sintering step may be used to reinforce the mechanical stability of the sample and tune its microstructure [12,13]. Behr et al. [12] and Delattre et al. [13] reported both channel spacing and porous matrix width decreased with the cooling rate, although these parameter designs can also be controlled by adding appropriate additives to the slurry. Additives can also reduce porous matrix width heterogeneity [12,13], which promotes uniform utilization of the active material (because of similar in-plane solid diffusion distance). The effects of additives on the solidification process, and eventually the channel geometry, are discussed in [28,29]. An exhaustive review of freeze-casting control can be found in [30]. Channels are less ordered when the freezing rate and solids loading in the slurry are increased, resulting in higher tortuosity factors, although it is still significantly lower compared with a non-structured electrode [12, 13, 14]. A lower area specific capacity has been measured for electrodes made with a lower freezing rate (thus, with lower tortuosity factor and larger channel width and spacing), at discharge rates of C/10, C/5, and 1C, which suggests solid-state diffusion is the rate-limiting transport mechanism for densely sintered NCA samples [13]. However, this result is expected to be strongly dependent on the porosity of the porous matrix, which is controlled partially by the sintering process for these monolithic electrodes, and cannot be generalized. At C/5, a high specific capacity is achieved for freeze-cast electrodes at a loading of ~15 $mAh.cm^{-2}$, while conventional electrodes are limited to around 5 $mAh.cm^{-2}$ [13].

Freeze-casting without post-processing sintering (sufficient mechanical strength allowed for direct assembling into cells) has been demonstrated for ultra-thick $LiCoO_2$ cathodes by Huang and Grant [14] and for ultra-thick graphite by Amin et al. [15]. Capacity retention (vs. 0.1C) at 5C was measured for a thin conventional slurry-casted (26 µm) $LiCoO_2$ electrode (72% of 0.5 $mAh.cm^{-2}$) compared with a freeze-cast ultra-thick (900 µm) $LiCoO_2$ cathode (59% of 14 $mAh.cm^{-2}$) [14]. Because no sintering was used, the fine-scale porosity was preserved and so was the lateral diffusion from the large pore channels into the finer microstructure and the surface area [14]. The better performance of the freeze-cast electrodes have been attributed to a lower tortuosity factor. SEM images after 200 cycles show no evidence of pulverization or large-scale fracture, corroborated with the high-capacity retention during cycling [14]. Ultra-thick (575–800 µm), high-porosity (50%) graphite exhibited relatively high discharge areal capacities of ∼18, ∼14, and∼7 mAh/cm^2 at C/10, C/5, and 1C, respectively, with good reproducibility [15]. To achieve mechanical integrity without sintering, only a small amount of binder was required (~5 wt. %). The authors attribute the decrease in capacity with the increasing C-rate (from C/10 to 1C) to the electrolyte diffusivity (ionic transport limitation), unlike the freeze-cast sintered NCA electrodes [13] (solid-state diffusion limitation). These ultra-thick electrodes may be difficult to incorporate in full cells intended for automotive applications because of technical issues, for example how to wind or fold them.

Lastly, freeze-tape-casting is a combination of the tape-casting process and freeze casting [16, 17, 18]. Contrary to batch-process freeze-casting, freeze-tape-casting is a continuous process which is more scalable. It has been applied to the manufacture of functionally graded ceramic microstructures

[16], lithium titanate oxide (LTO) [17], and sulfur−graphene-oxide (S-GO) electrodes [18]. The specific capacities of baseline tape-cast (34% porous) and freeze-tape-cast (75% porous) LTO electrodes with a similar loading of 4.5 mg.cm^{-2} were measured, respectively, at ~105 and ~130 mAh.g^{-1} at 1C [17]. Higher capacities were systematically measured for the freeze-tape-cast electrode from 0.1 to 1C. Almost doubling the loading (4.5 to 8.8 mg.cm^{-2}) with the same high porosity had minimal impact on the achieved freeze-tape-cast electrode capacity (130 to 125 mAh.g^{-1}) [17]. Freeze tape cast S−GO electrodes also exhibited better capacity retention compared to the baseline tape cast electrodes, ~52% vs. 38% at 3.0 mA.cm^{-2}, even though they had a slightly higher loading (~2.0 mg.S.cm^{-2} vs. 1.7 mg.S.cm^{-2}) [18]. Better rate performances were attributed to the continuously 3D 3D-aligned pore structure that provides more facile pathways to the active sulfur [18]. Furthermore, the authors claimed the wide interlayer spacing granted by the freeze-tape-cast process prevented the obstruction of diffusion paths that may occur because of sulfur deposition during cell operation (polysulfide shuttle effect) [18]. Also, compression induced by coin cell assembly decreased the size of the electrode to 60% of its original thickness but its aligned pore structure was preserved [18]. The tortuosity factors before/after compression were not computed to verify this statement, rather a visual inspection was used to make this intermediate thick determination. The freeze-tape-casting technique is also currently being considered to tailor graphite anodes of intermediate thicknesses (cf. Fig. 1) specifically for fast-charge applications because a lower tortuosity is expected to mitigate electrolyte depletion and lithium plating under fast charge. Here, graphite was combined with a binder and carbon black in the slurry used for the freeze tape casting experiment to make electrodes similar to conventional ones used in lithium-ion batteries.

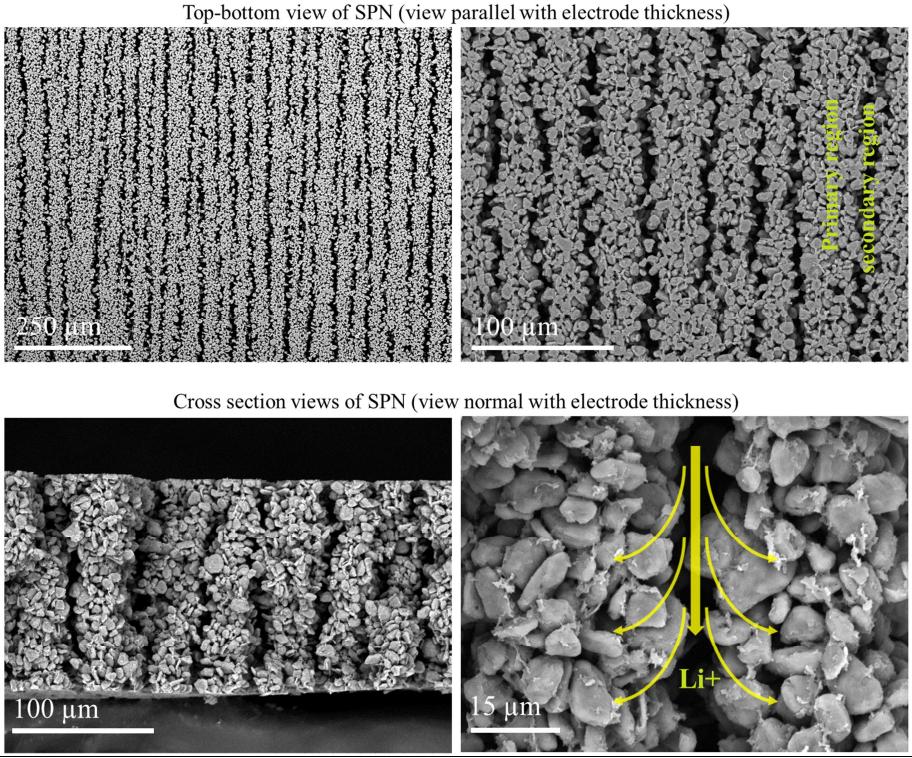

Figure 1. SEM images at different magnifications of a superior graphite anode manufactured with

freeze-tape-casting at Lawrence Berkeley National Laboratory. Electrode is ~150 µm thick with a porosity of 58% and a theoretical areal capacity of 4.5 mAh.cm^{-2} (no calendering, no sintering). Current work is focused on achieving higher density. Primary (channel spacing) and secondary region (channel width) are, respectively, 28 ± 7 µm and 8 ± 3 µm wide.

Channel architectures have also been employed, in a different manner, as current collectors for lithium metal electrodes [31]. Here, the channel walls' function is to guide the lithium stripping and plating process and to confine the volume change, while channels are filled with lithium metal. The SPN architectures are not limited to the battery field as they have also been investigated for solid oxide fuel cells [16,32,33,34,35] and other applications [19,20, 36,37].

All of these approaches rely on the same idea—creating large, straight pore 1D channels or pathways oriented along the electrode thickness to improve the through-plane ionic diffusion. While the optimization objective is to reduce the through-plane tortuosity, constraints have to be considered on the porous matrix density and width to prevent solid-state diffusion from becoming the rate-limiting mechanism, especially for freeze-cast electrodes that undergo a post-processing sintering step [13]. What the results reported by these different groups [7,8,9,13,17,22,23,24,25] have in common are better performance with structured electrodes compared to standard electrodes only under relatively high C-rate and/or for thick electrodes. Indeed, reducing the tortuosity factor improves the electrochemical performances of the cell only when transport limitations are significant. Such alternative electrode architectures are then particularly adequate for automotive applications (intermediate-thickness electrodes at fast charge rates) and for stationary energy storage (ultra-thick electrodes at low C-rates).

These techniques are not equivalent. Particle magnetic alignment [22] is only suitable for anisotropic materials and offers no control because it roughly consists in a sample rotation (particle alignment, rather than incorporating a secondary pore network). Magnetic templating [7] and iterative co-extrusion [8] generate cylindrical channels, with a finer control of the channel dimension and location for the latter. Co-extrusion [23,24,25] and laser-ablation [9] provide rectangular channels (grooves) and fine control of the geometry. Lastly, freeze-casting and its variants [12,13,14,15,16,17,18] generate structures whose shape depends on the solvent and conditions used with overall control of the structure dimension. Water-processing often results in acicular/lamellar pores, but tert-butyl alcohol gives hexagonal-shaped pores due to the different crystal growth habits. For freeze-tape-casting, however, water is the most commonly used solvent. Lamellae topologies are complex, heterogeneous, and not continuous (contrary to the grooves obtained with co-extrusion), but sometimes present bridges connecting adjacent lamellar walls [13,29]. However, SEM images, which are two-dimensional, can be somewhat deceiving to judge of 3D structures. Additives have to be chosen carefully to achieve the desired geometry [28,29], complexifying the manufacturing process, even though in the absence of a sintering step that burn out additives, only a minimal amount of additives is used not to interfere with performance. Composite electrodes made with freeze tape casting are very much like conventional electrodes with active material, binder and conductive carbon cast together, except that the tape casting bed is cold, and freeze-drying is used to remove solvent afterwards. Lastly, freeze-casting allows

the manufacturing of ultra-thick electrodes (900 µm), which is not achievable with standard slurry-casting techniques [14].

Results from [7,8,13,25] indicate that minimizing the electrode tortuosity requires optimizing the porosity repartition between the aligned pore channels and the porous microstructure as well as the spacing between the channels. In this work, we propose an SPN design optimization based upon an analytical tortuosity factor model that considers only the impact of SPN on ionic diffusion. This model has been used to provide SPN design recommendations for different electrode materials and geometry channels (representative of cylindrical, rectangular, and, to a certain extent, lamellar channels) to minimize the through-plane tortuosity factor while keeping a high-enough diffusion within the porous matrix.

Compared to other modeling works [8, 11, 23, 24, 25], this article investigates a large design space detailed in table 4. Channel geometries, channel dimension (volume, width and thickness ratios), unilayer and bilayer structured electrodes, and exhaustive tortuosity parameter space including anisotropy and impact of additives are all considered and optimal design parameters are deduced through optimization objectives functions introduced in §3.3 which are not considered elsewhere to the author's knowledge.

Table 1. Methods used to create secondary pore network.

Technique investigated (experiment/modeling)	**Electrode material, thickness, and porosity**	**Pore network, channel spacing w_1, channel width w_2**	**Primary results**	**References**
Magnetic particle alignment with iron-oxide nanoparticles sacrificial material (Y/N)	Anisotropic graphite, 200 µm, 32%–45%	Rotation of anisotropic flake-like particles, *n/a*, *n/a*	Tortuosity factor reduced by a factor of 4. Capacity increased by a factor of 3 (5 mg graphite.cm^{-2}) and 1.6 (9.1 mg graphite.cm^{-2}) at 1C.	[22]
Magnetic templating with emulsion droplets of a ferrofluid sacrificial material (Y/N)	$LiCoO_2$, 310 µm, 39%–40%	Cylindrical channels, 18–58 µm, 3–8 µm	Pore-channel diameter less uniform with emulsion droplets. Capacity increased by a factor of 3 at 2C, modified by pore-channel spacing (smaller pore spacings are superior). Near complete utilization of electrode capacity during dynamic stress test.	[7]
Magnetic templating with nylon microrods coated with superparamagnetic iron-oxide nanoparticle sacrificial material (Y/N)	$LiCoO_2$, 310 µm, 39%–42%	Cylindrical channels, 28–32 µm, 5–15 µm		
	$LiCoO_2$, 220 µm, 31%–32%	Cylindrical channels, 24–30 µm, 5–15 µm		
Iterative co-extrusion and sintering (Y/Y)	$LiCoO_2$, 220 µm, 30%–38%	Cylindrical channels, 1320 µm, 680 µm / 120 µm, 60 µm / 11 µm, 6 µm	Channel volume ratio and channel spacing normalized with thickness control tortuosity factor. Capacity increased by a factor of 3 at 1–2C with smaller channels.	[8]
Co-extrusion (N/Y)	$LiCoO_2$, 150–400 µm, 34%	Rectangular channels, w_1/w_2=0.83–20 and w_i=25–300 µm	Volumetric capacity reach maximum for w_1/w_2 ~3–5 at 1C. Capacity increased by a factor 1.5–5 for ultra-thick electrode. Higher current density heterogeneity, controlled by edge sharpness.	[23]
Co-extrusion (N/Y)	NMC, 60–170 µm, 33%	Rectangular channel, w_1/w_2=4 and 9 with w_2=25 µm	Bilayer architecture (thin layer w/o SPN, thick layer w/ SPN) increase gravimetric and volumetric energy at 1C.	[24]
Co-extrusion (N/Y)	Full cell: $LiCoO_2$, 50–200 µm, 30% and graphite 50–200 µm, 30%	Rectangular channel	Low channel spacing normalized with thickness ratio is recommended. SPN volume ratio of 15–25% recommended. Higher capacity retention when both electrodes are architectured.	[25]
Ultrafast laser ablation	NMC, 52–258 µm,	Rectangular channels,	Capacity retention increased from ~50% to	[9]

(Y/N)	47%–53%	200 µm, 15–30 µm	65% for a 100-µm-thick electrode at 1C.		
Ultrafast laser ablation (Y/N)	NMC, 100–210 µm, 26%–50%	Rectangular channels, 200 µm, 30 µm	Capacity retention increased from ~12% to 50% for a 100-µm-thick electrode at 2C.		[10]
Ultrafast laser ablation (Y/Y)	Full cell: unstructured NMC and structured graphite, 64 µm, 35% (before laser ablation)	Cylindrical channel, 70 µm, 20 µm.	Heterogeneity of laser-induced structures due to particle sizes and shape heterogeneity. Structured anode provides maximum improvement in the range 1–3 C while the unstructured cathode is limiting at higher rate. Higher capacity retention after cycling (85% vs. 75% at 1C 1000 cycles).		[11]
Microstructure mechanical milling (Y/Y)	Activated carbon, 50-200 µm, 75% before machining	Rectangular channels, 400 µm, 100 µm	Significant enhanced areal capacitance for thick electrode at high rate		[19]
Freeze-casting with sintering (Y/N)	NCA, 600–700 µm, 30%–50%	Lamellar channels	Zigzag-shaped pore channel for cooling rate > 1 °C/min and/or for solid loading within the slurry > 30 vol-%.	Channel dimension and spacing decrease with cooling rate.	[12]
Freeze-casting with sintering (Y/N)	NCA, 300–330 µm, 45%	Lamellar channels, 8–24 µm, 7–19 µm with $1 < w_1/w_2 < \sim 1.25$	Reduced tortuosity from ~2.8 to ~1.5–2.5, lower values with lower cooling rate.		[13]
Freeze-casting without sintering (Y/N)	$LiCoO_2$, 900 µm, 44%	Coral-like structure. Pore size 4–7 µm.	Reduced tortuosity from 3.2 to 1.7. Structure integrity during cycling. Better capacity retention compared with thinner slurry casted electrode.		[14]
Freeze-casting without sintering (Y/N)	Graphite, 575–800 µm, 50%	Lamellar channels, 16.6 ±3.3 µm, 8.8 ±1.4 µm	At low C-rate (C/10) 800-µm-thick structured electrode can be cycled without ionic diffusion limitation.		[15]
Freeze-tape-casting without sintering (Y/N)	LTO, 80–150 µm, 74%–75%	Lamellar channels, 6–9 µm, 7–8 µm	Freezing temperature impacts capacity loss.		[17]
Freeze-tape-casting without sintering (Y/N)	sulfur–graphene oxide, 200–300 µm	Lamellar channels, ~5 µm, 10–20 µm,	Wide interlayer spacing prevents polysulfide shuttle effect to obstruct pores. Compression assembly preserved pore alignment.		[18]

3. Secondary-pore network tortuosity factor analytical model

Parameters used in this model are listed in Table 2. A cross-section schematic of the structured geometry and of the unstructured (baseline) geometry are shown in Fig. 2. A top-bottom view of the channel geometry is shown in Fig. 3. The analytical model presented here is available on open source online [38].

Table 2. Nomenclature

Symbol	Parameter
w	Width [m]
L	Thickness [m]
A	In-plane area [m^2]
V	Volume [m^3]
ε	Volume fraction
k	CBD volume fraction ratio of active material volume fraction
τ	Tortuosity factor
$\tau^{tp/ip}$	Through-plane in-plane anisotropy ratio
γ, α	Respectively, pre-factor and exponent coefficient of generalized Archie's empirical law

a, b	Tortuosity factor CBD corrective coefficients of eq. 7
D	Diffusion coefficient [$m^2.s^{-1}$]
D_0	Bulk or dense diffusion coefficient [$m^2.s^{-1}$]
D_n	Normalized diffusion coefficient
t	Characteristic diffusion time [s]
R_w	Secondary region width to primary region width ratio w_2/w_1
R_V	Volume fraction of secondary region $V_2/(V_1+V_2)$
R_t	Width-to-thickness ratio of primary region w_1/L
R_L	Primary region thickness ratio, only for bilayer structured electrode $L/(L+L_I)$
N	Number of primary regions ($n \gg 1$)

Subscript	**Indication**
1	Primary region (porous matrix)
2	Secondary region (channel)
3	Third region (porous pad), only for bilayer structured electrode
$I-II$	Layer that contains primary and secondary region, notation used only for bilayer structured electrode
III	Layer that contains third region, only for bilayer structured electrode
tot	Whole electrode, structured
base	Whole electrode, unstructured
E	Electrolyte domain
AM	Active material domain
CBD	Carbon binder domain
g	Gain

Superscript	**Indication**
ip	Along in-plane direction
tp	Along through-plane (thickness) direction

3.1 Structured electrode

Figure 2 represents the investigated geometry of the structured electrode with an SPN and that of the unstructured (baseline) electrode. Structured electrodes exist in two variants: without (unilayer case) or with (bilayer case) a small pad of porous electrode without an SPN at the base of the current collector side, as described in [24].

3.1.1 Unilayer case

The primary region (also called the porous matrix) contains pores, active material, and CBD, while the secondary region is completely filled with electrolyte, then:

$$\begin{gathered}\varepsilon_{E,1} + \varepsilon_{AM,1} + \varepsilon_{CBD,1} = 1 \\ \varepsilon_{CBD,1} = k \times \varepsilon_{AM,1}, \forall \varepsilon_{AM,1} \text{ then } \varepsilon_{AM,1} = \frac{1-\varepsilon_{E,1}}{1+k} \\ \varepsilon_{E,2} = 1, \varepsilon_{AM,2} = \varepsilon_{CBD,2} = 0\end{gathered} \quad [3]$$

With $\varepsilon_{E,1}$, $\varepsilon_{AM,1}$, $\varepsilon_{CBD,1}$, respectively, the porosity, active material volume fraction, and CBD volume fraction within the primary region; and $\varepsilon_{E,2}$, the porosity within the secondary region. The CBD weight ratio is constant so its volume fraction is a ratio of the active material volume fraction. Figure 3 shows the two channel geometries considered in this work. The rectangular channels (grooves), cf. Fig. 3a, is representative of co-extrusion [23,24,25] and ultrafast laser ablation [9]. If the laminar structure obtained with freeze-casting is free of bridges and well aligned, this geometry also applied. The cylindrical channels, cf. Fig. 3b, is representative of iterative co-extrusion, sintering technique [8], and magnetic templating [7]. The region's volume depends on the channel geometry:

$$V_1 = A_1 \times L \text{ with } A_1 = \begin{cases} w_1 \times W \times n & \text{if channels are rectangular} \\ (w_1 + w_2)^2 \times n^2 - A_2 & \text{if channels are cylindrical} \end{cases} \quad [4a]$$

$$V_2 = A_2 \times L \text{ with } A_2 = \begin{cases} w_2 \times W \times (n-1) & \text{if channels are rectangular} \\ \pi \times \left(\frac{w_2}{2}\right)^2 \times n^2 & \text{if channels are cylindrical} \end{cases} \quad [4b]$$

where w_1 and w_2 are the width, V_1 and V_2 are the volume, and A_1 and A_2 are the in-plane area of, respectively, the primary and secondary regions. The electrode dimension normal to the figure 2 system of axis is noted as *W*. The model is insensitive with *W* because it simplifies with volume region ratio. The number of primary regions is noted as *n,* while we consider the electrode in-plane extremities are primary regions. Its value is chosen extremely high to consider a full-size electrode. Because of this, model results are insensitive with *n* because it simplifies with volume region ratio. The electrode thickness is noted as *L*. The total volume fractions are obtained by a rule of mixture:

$$\varepsilon_{i,tot} = \frac{\sum_{k=1}^{N} \varepsilon_{i,k} \times V_k}{\sum_{k=1}^{N} V_k} \text{ with } i = E, AM \text{ or } CBD \text{ and } N=2 \quad [5]$$

Along the electrode thickness (through-plane direction), the primary region and secondary region are parallel. Then the normalized effective through-plane diffusion coefficient $D_{n,tot}^{tp}$ is deduced from a simple rule of mixture for parallel paths [39]:

$$D_{n,tot}^{tp} = \frac{\sum_{k=1}^{2} D_{n,k}^{tp} \times V_k}{\sum_{k=1}^{2} V_k} \quad [6a]$$

with $D_{n,k}^{tp}$ the normalized effective through-plane diffusion coefficient of the region *k,* deduced from equation 1, (i.e., $D_{n,k}^{tp} = \varepsilon_{E,k} / \tau_k^{tp}$). The rule of mixture assumes there is no transversal exchange between the primary and secondary region (flux is one-dimensional, along the electrode thickness).Normalized diffusion coefficients along a given direction are defined as the ratio of the effective diffusion coefficient of the medium embedded in a composite structure along this same direction over the diffusion coefficient of the dense medium. Because the secondary region is completely filled with electrolyte, its normalized effective diffusion coefficient, $D_{n,2}^{tp}$, $D_{n,2}^{ip}$, and its

tortuosity factor, τ_2^{tp}, τ_2^{ip}, are both equal to 1. Because $D_{n,tot}^{tp}$ is volume averaged, local variation due to electrode heterogeneity does not impact its value as long as $\langle V_k \rangle$ and $\langle D_{n,k}^{tp} \times V_k \rangle$ (<*> is the average of *) are conserved. Previous work [27] has shown tortuosity factor depends on the porosity and on the CBD volume fraction and morphology. Equation 7a, deduced from figure 7b of reference 24, has been determined with a corrective term, $a * \varepsilon + b$, which takes into consideration the impact of the CBD on the ionic diffusion. As CBD is often not distinguishable from the pore with X-ray computed tomography, homogenization calculation performed on the combined pore and CBD domain (of volume fraction $\varepsilon_{E,1} + \varepsilon_{CBD,1}$) can be corrected using equation 7a. Combining equations 7a and 3, $\varepsilon_{CBD,1}$ is replaced with the constant k (cf. eq. 7b). The notation, τ_ε, of equation 7b is used later in Table 3 to reduce expression length.

$$\tau_1^{tp} = \left(a \times \varepsilon_{E,1} + b\right) \times \gamma \times \left(\varepsilon_{E,1} + \varepsilon_{CBD,1}\right)^{1-\alpha} \quad [7a]$$

$$\tau_{\varepsilon_{E,1}} = \tau_1^{tp} = \left(a \times \varepsilon_{E,1} + b\right) \times \gamma \times \left(\frac{\varepsilon_{E,1} + k}{1 + k}\right)^{1-\alpha} \quad [7b]$$

Several authors have shown lithium-ion electrode effective diffusion is anisotropic because of the active material particles morphology [26, 27]. High through-plane tortuosity factor is often derived from high tortuosity anisotropy induced by misaligned non-spherical particles that extend the through-plane diffusion path [22, 27]. Therefore, it is important to consider tortuosity anisotropy when modeling electrode with high through-plane tortuosity as both are usually linked. In this model, diffusion anisotropy is considered using a tortuosity factor anisotropy coefficient, $\tau^{tp/ip} = \tau^{tp}/\tau^{ip}$. We assume $\tau^{tp/ip}$ is the same for the baseline unstructured electrode and for the primary region of the structured electrode (i.e., diffusion anisotropy for a given microstructure morphology does not change with porosity). In-plane tortuosity factor and normalized effective diffusion coefficient of the primary region are then deduced as:

$$\tau_1^{ip} = \frac{\tau_1^{tp}}{\tau^{tp/ip}} \text{ and } D_{n,1}^{ip} = \frac{\varepsilon_{E,1}}{\tau_1^{ip}} \quad [8]$$

Lastly, electrode through-plane characteristic diffusion time, t_{tot}^{tp}, and primary region in-plane characteristic diffusion time, t_1^{ip}, are calculated considering, respectively, the electrode thickness L and the distance macropore wall to primary region center (i.e., $w_1/2$) as their characteristic length:

$$t_{tot}^{tp} = \frac{L^2}{D_{tot}^{tp}} \text{ and } t_1^{ip} = \frac{{w_1}^2}{4D_1^{ip}} \quad [9]$$

with D_{tot}^{tp} and D_1^{ip} the effective electrode through-plane diffusion coefficient and the effective primary region in-plane diffusion coefficient. If not specified otherwise, model results are obtained considering the unilayer case.

3.1.2 Bilayer case

Bilayer architecture corresponds to the geometry investigated by Cobb and Solberg [24]. The layer noted III is closer to the current collector and includes the third region. The second layer, noted $I - II$, is closer to the separator and includes the primary and secondary regions as described in the

unilayer case. In this model, the primary and third regions share the same volume fractions, tortuosity, and diffusion coefficients. The volume of the third region is given by equation 4c, and equation 5 can be re-used, but with *N=3*.

$$V_3 = (A_1 + A_2) \times L_{III} \quad [4c]$$

Because layers a and b are in series, and primary and secondary regions are in parallel, there are two possible ways to calculate the normalized effective through-plane diffusion coefficient, $D_{n,tot}^{tp}$, that will bound its actual value. The first approach consists in homogenizing first regions 1 and 2 (parallel law [39]) and then homogenize it with region 3 (serial law [39]) and provides upper bound $D_{n,tot}^{tp*}$:

$$D_{n,b}^{tp} = \frac{\sum_{k=1}^{2} D_{n,k}^{tp} \times V_k}{\sum_{k=1}^{2} V_k} \text{ then } \frac{1}{D_{n,tot}^{tp*}} = \frac{\frac{V_1 + V_2}{D_{n,b}^{tp}} + \frac{V_3}{D_{n,3}^{tp}}}{V_1 + V_2 + V_3} \quad [6b]$$

The second approach consists in homogenizing first regions 1 and 3, and region 2 and 3 (serial law), and then homogenize their results (parallel law), which provides lower bound $D_{n,tot}^{tp**}$:

$$\frac{1}{D_{n,23}^{tp}} = \frac{\frac{V_2}{D_{n,2}^{tp}} + \frac{A_2 L_{III}}{D_{n,3}^{tp}}}{V_2 + A_2 L_{III}} \text{ then } D_{n,tot}^{tp**} = \frac{D_{n,1}^{tp} A_1 + D_{n,23}^{tp} A_2}{A_1 + A_2} \quad [6c]$$

Electrode through-plane characteristic diffusion time, t_{tot}^{tp}, is obtained using the electrode thickness $L + L_{III}$ as characteristic length. Results obtained from the two approaches will be compared in Appendix C. If $L_{III} = 0$, then the electrode is actually a unilayer and $D_{n,tot}^{tp} = D_{n,tot}^{tp*} = D_{n,tot}^{tp**}$.

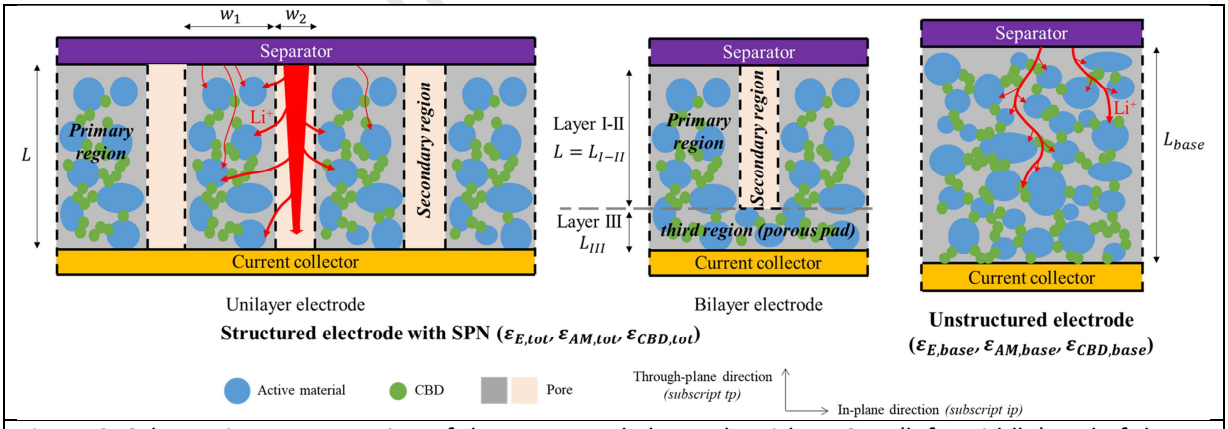

Figure 2. Schematic representation of the structured electrode with an SPN (left, middle) and of the unstructured baseline electrode (right).

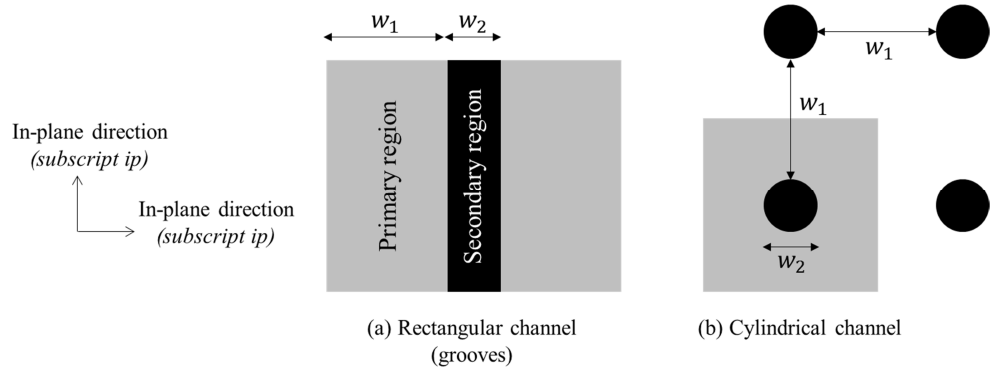

Figure 3. Schematic representation of the large pore channels: (a) with a rectangular (grooves) geometry, and (b) with a cylindrical geometry.

3.2 Comparison with the baseline electrode

To provide a meaningful comparison, electrodes with and without an SPN must be compared at the same theoretical capacity, which implies the mass of active materials must be identical:

$$\varepsilon_{AM,1} \times (V_1 + V_3) = \varepsilon_{AM,base} \times V_{base} \quad [10a]$$

$$\varepsilon_{AM,tot} \times (V_1 + V_2 + V_3) = \varepsilon_{AM,base} \times V_{base} \quad [10b]$$

$$\frac{A_{base} L_{base}}{A_1 L + (A_1 + A_2) L_{III}} = \frac{\varepsilon_{AM,1}}{\varepsilon_{AM,base}} \quad [10c]$$

with $\varepsilon_{AM,base}$ and V_{base}, respectively, the volume fraction of the active material within the baseline, unstructured, electrode and the baseline electrode volume. Note that equations 10a, 10b, and 10c are equivalent. Assuming both electrodes share the same area (i.e., $A_{base} = A_1 + A_2$), then three approaches are possible to enforce equation 10c.

First, keeping the same electrode volume (and thus thickness) but densifying the primary region to compensate for the total porosity increase induced by the pore channels: $L + L_{III} = L_{base}$ then $\varepsilon_{E,1} < \varepsilon_{E,base}$. This case preserves the theoretical volumetric and gravimetric specific capacity but penalizes the primary region ionic diffusion coefficient and diffusion time compared with the baseline electrode, which may result in an in-plane diffusion limitation within the primary region. Achieving this condition in practical is highly dependent on the manufacturing technique. If the SPN manufacturing technique removes active material from the electrode (e.g., laser ablation), then electrodes can be prepared with different active material loadings or calendering pressures to match the baseline electrode porosity $\varepsilon_{E,base}$ for the unstructured electrode, and the primary region porosity $\varepsilon_{E,1}$ for the to-be structured electrode. Target porosity values, $\varepsilon_{E,base}$ and $\varepsilon_{E,1}$, can be deduced form figure 5, considering the SPN volume ratio is know in advance as it is controllable (more or less depending of what technique is used, as discussed in the review section of the article). On the contrary, if the SPN manufacturing technique does not remove active material but spatially redistribute active material (e.g., freeze casting), then both the unstructured electrode and the to-be structured electrode should be prepared with same thickness and initial porosity.

Second, keeping the same porosity within the porous matrix but increasing the electrode volume: $\varepsilon_{E,1} = \varepsilon_{E,base}$ then $L + L_{III} > L_{base}$. This case preserves the theoretical gravimetric-specific capacity neglecting electrolyte weight and the primary region ionic diffusion coefficient, but penalizes the primary region through-plane diffusion time and the theoretical volumetric specific capacity compared with the baseline electrode. Lastly, a mixed approach is possible, varying both thickness and primary region porosity. If not specified otherwise, model results are obtained considering both structured and baseline electrodes share the same thickness (i.e., first approach with same theoretical volumetric and gravimetric-specific capacity). The second approach is considered in Appendix B. The third approach is not considered in this work. Tortuosity anisotropy is assumed identical between the primary region and the baseline electrode. The CBD weight ratio is identical between the structured and unstructured electrode.

The choice to compare structured and baseline electrodes using a constant thickness or porosity depends on the context. For volume and mass constrained battery systems, it makes sense to compare at identical thickness; otherwise, relaxing the thickness constraint prevents increasing electrolyte transport resistance within the primary region.

3.3 SPN optimization objectives

The optimization objectives formulated below have in common relying on a balance between improving electrode through-plane diffusion, $D_{n,tot}^{tp}$, and degrading primary region in-plane diffusion, $D_{n,1}^{ip}$. Adding large pore channels enhances the effective through-plane diffusion of the electrode as the secondary region volume become predominant compared with the other regions (i.e., $V_2 \gg V_1, V_3$) which implies the electrode through-plane diffusion is mostly controlled by the secondary region diffusion coefficient (i.e., $D_{n,tot}^{tp} \approx D_{n,2}^{tp} = 1$, cf. eq. 6a, 6b, 6c). Although, as discussed in §3.2, to preserve the theoretical volumetric specific capacity between the structured and unstructured electrodes, the SPN must be compensated with an increase of the active material within the porous matrix $\varepsilon_{AM,1}$ and, thus, a decrease of the primary region porosity $\varepsilon_{E,1}$, an increase of the primary region tortuosity factor τ_1^{tp} and τ_1^{ip}, which eventually results in a decrease of the normalized effective diffusion coefficient of the primary region, both through plane $D_{n,1}^{tp}$ and in-plane $D_{n,1}^{ip}$. While the decrease of $D_{n,1}^{tp}$ is not problematic because the role of the secondary region is precisely to reduce transport resistance all along the electrode thickness, a decrease of $D_{n,1}^{ip}$ will aggravate in-plane (transversal) heterogeneities because active material utilization at the center of the primary region is reduced due to electrolyte transport resistance. Nonuniform in-plane utilization of the active material and potential electrolyte depletion/saturation in the center of the primary region is expected to reduce actual capacity and can trigger earlier degradations.

3.3.1 Maximize diffusion gain product

Electrode through-plane diffusion (tortuosity factor) gain, $D_{tot,g}^{tp}$ ($\tau_{tot,g}^{tp}$), and primary region in-plane diffusion (tortuosity factor) gain, $D_{1,g}^{ip}$ ($\tau_{1,g}^{ip}$), are defined as:

$$D_{tot,g}^{tp} = \frac{D_{n,tot}^{tp}}{D_{n,base}^{tp}} > 1 \text{ and } \tau_{tot,g}^{tp} = \frac{\tau_{tot}^{tp}}{\tau_{base}^{tp}} < 1 \quad [11a]$$

$$D_{1,g}^{ip} = \frac{D_{n,1}^{ip}}{D_{n,base}^{ip}} < 1 \text{ and } \tau_{1,g}^{ip} = \frac{\tau_{1}^{ip}}{\tau_{base}^{ip}} > 1 \quad [11b]$$

Note that the electrode through-plane diffusion gain is above 1, while the primary region in-plane diffusion gain is below 1. An above 1 diffusion gain indicates an improvement, while an above 1 tortuosity gain is a deterioration. Since both electrode through-plane diffusion and primary region in-plane diffusion must be high enough, a possible compromise is to find the SPN design parameters that maximize the gain product, $D_{tot,g}^{tp} \times D_{1,g}^{ip}$, for a given total volume fractions, which defines the first optimization objective.

3.3.2 Enforce isotropic diffusion coefficient

Being restricted to a simple diffusion approach, the model doesn't indicate how to prioritize the electrode through-plane diffusion coefficient compared with the primary region in-plane diffusion coefficient. Considering both should be sufficiently high, a neutral approach that does not favor one direction over another is considered here. The optimization objective consists in finding the design parameters that verify $D_{n,tot}^{tp}/D_{n,1}^{ip} = 1$ for given total volume fractions, i.e. a structured electrode with diffusion isotropy between the electrode through-plane diffusion coefficient and the primary region in-plane diffusion coefficient. This objective aims to balance the diffusion, preventing excessively favoring one direction over another *without considering diffusion distance*.

3.3.3 Enforce isotropic characteristic diffusion time

The neutral (i.e. isotropic) approach proposed in the previous paragraph is kept but applied to characteristic diffusion time instead of diffusion coefficient. The third optimization objective consists in finding the design parameters that verify $t_{tot}^{tp} = / t_1^{ip} = 1$, with t_{tot}^{tp} the electrode through-plane characteristic diffusion time and t_1^{ip} the primary region in-plane characteristic diffusion time defined in equation 9. For the unilayer case, such condition translates in a particular value for the ratio of the electrode through-plane diffusion coefficient over the primary region in-plane diffusion coefficient (cf. eq. 12a), which means the second optimization objective is a particular case ($w_1/L = 2$) of the third optimization objective. Among the three optimization objectives proposed in this work, this one considers the electrode thickness L and the primary region width w_1 as variables, which allows one to provide design recommendations as a function of electrode thicknesses.

$$\frac{t_{tot}^{tp}}{t_1^{ip}} = 1 \;\Rightarrow \frac{D_{tot}^{tp}}{D_1^{ip}} = \frac{D_{n,tot}^{tp}}{D_{n,1}^{ip}} = \frac{4 \times L^2}{{w_1}^2} \quad [12a]$$

3.4 SPN design parameters

For the simple unilayer case, regions are parallel so that a rule of mixture can be applied to deduce the effective diffusion coefficient (cf. eq. 6a). This indicates that the volume region ratio, rather

than the volume region values taken individually, is a key parameter. However, to choose relevant design parameters with regard to the chosen optimization objectives, all of the independent variables involved in their expressions must be identified first. These expressions are provided in table 3, considering the unilayer case. Equations 3 and 10c are used to replace the primary region porosity with the electrode baseline porosity for the case thickness is preserved between the baseline and the structured electrode (cf. eq. 13). The volume fraction of the secondary region noted R_V is introduced to simplify equations (cf. eq. 14). Expressions are different depending on how baseline and structured electrodes are compared (cf. §3.2). Equations deduced from the two proposed tortuosity expressions are equivalent if no carbon-binder is considered (i.e., eq. 15–18a are equivalent with 15–18b for a = 0, b = 1, and k = 0, cf. eq. 3 and 7).

$$\frac{1-\varepsilon_{E,1}}{1+k} = \frac{1-\varepsilon_{E,base}}{1+k} \times \frac{V_1+V_2}{V_1} \Rightarrow \varepsilon_{E,1} = \left(\varepsilon_{E,base}-1\right)\left(\frac{V_1+V_2}{V_1}\right)+1 = \frac{\varepsilon_{E,base}-1}{1-R_V}+1 \quad [13]$$

$$R_V = \frac{V_2}{V_1+V_2} \quad [14]$$

Table 3. Expressions of the optimization functions for unilayer case. [1]Corresponds to $L + L_{III} = L_{base}$ then $\varepsilon_{E,1} < \varepsilon_{E,base}$. [2]Corresponds to $\varepsilon_{E,1} = \varepsilon_{E,base}$ then $L + L_{III} > L_{base}$.

	Tortuosity expression τ^{tp}	Comparison	Expression		Independent variables
Diffusion gain product $D_{tot,g}^{tp} \times D_{1,g}^{ip}$	$(a\varepsilon_E + b) \times \gamma(\varepsilon_E + \varepsilon_{CBD})^{1-\alpha}$	Same thickness[1]	$\left(\frac{\varepsilon_{E,1}}{\tau_{\varepsilon_{E,1}}}(1-R_V)+R_V\right)\frac{\varepsilon_{E,1}}{\tau_{\varepsilon_{E,1}}}\left(\frac{\tau_{\varepsilon_{E,base}}}{\varepsilon_{E,base}}\right)^2$	[15a]	$\varepsilon_{E,base}$ R_V α, γ a, b, k
		Same porosity[2]	$R_V\left(\frac{\tau^{tp}_{\varepsilon_{E,base}}}{\varepsilon_{E,base}}-1\right)+1$	[16a]	
	$\gamma{\varepsilon_E}^{1-\alpha}$	Same thickness[1]	$\left[\left(\frac{\varepsilon_{E,base}-1}{1-R_V}+1\right)^{\alpha}\frac{1-R_V}{\gamma}+R_V\right] \times \left[\left(\frac{\varepsilon_{E,base}-1}{1-R_V}+1\right)^{\alpha}\frac{\gamma}{{\varepsilon_{E,base}}^{2\alpha}}\right]$	[15b]	$\varepsilon_{E,base}$ R_V α, γ
		Same porosity[2]	$R_V\left(\gamma{\varepsilon_{E,base}}^{-\alpha}-1\right)+1$	[16b]	
Diffusion ratio $\frac{D_{n,tot}^{tp}}{D_{n,1}^{ip}}$	$(a\varepsilon_E + b) \times \gamma(\varepsilon_E + \varepsilon_{CBD})^{1-\alpha}$	Same thickness[1]	$\frac{R_V\left(\frac{\tau_{\varepsilon_{E,1}}}{\varepsilon_{E,1}}-1\right)+1}{\tau^{tp/ip}}$	[17a]	$\varepsilon_{E,base}$ R_V α, γ a, b, k $\tau^{tp/ip}$
		Same porosity[2]	$\frac{R_V\left(\frac{\tau^{tp}_{\varepsilon_{E,base}}}{\varepsilon_{E,base}}-1\right)+1}{\tau^{tp/ip}}$	[18a]	
	$\gamma{\varepsilon_E}^{1-\alpha}$	Same thickness[1]	$\left[\left(\frac{\varepsilon_{E,base}-1}{1-R_V}+1\right)^{\alpha}\frac{1-R_V}{\gamma}+R_V\right] \times \left[\left(\frac{\varepsilon_{E,base}-1}{1-R_V}+1\right)^{-\alpha}\frac{\gamma}{\tau^{tp/ip}}\right]$	[17b]	$\varepsilon_{E,base}$ R_V α, γ $\tau^{tp/ip}$
		Same porosity[2]	$\frac{R_V\left(\gamma{\varepsilon_{E,base}}^{-\alpha}-1\right)+1}{\tau^{tp/ip}}$	[18b]	

Expressions for the first optimization objective (diffusion gain product) are provided in equations 15–16 in table 3. Note that the tortuosity anisotropy $\tau^{tp/ip}$ simplifies, indicating it is not a

design parameter for maximizing the diffusion gain product. The diffusion gain product, $D_{tot,g}^{tp} \times D_{1,g}^{ip}$, is a function of the baseline porosity $\varepsilon_{E,base}$ (and of the CBD volume fraction ratio of active material volume fraction *k* if CBD is considered), the through-plane tortuosity factor coefficients (γ, α and a, b if CBD is considered), and of the volume fraction of the secondary region, R_V. Therefore, for a given baseline electrode and given tortuosity coefficients, the only design parameter to maximize the diffusion gain product is R_V. Alternatively, the secondary-region-width to primary-region-width ratio, R_w, can be considered instead of R_V (cf. eq. 19). However, since different width ratios are required to achieve the same secondary region volume fraction with rectangular or cylindrical channels (cf. eq. 4a, 4b), R_w design recommendations depend on the channel shape and are then less generic than those obtained with R_V (i.e., $\{R_w, \text{channel geometry}\}$ is a bijection of $\{R_V\}$).

$$R_w = \frac{w_2}{w_1} \qquad [19]$$

Expressions of the ratio between the electrode through-plane diffusion coefficient and the primary region in-plane diffusion coefficient, $D_{n,tot}^{tp}/D_{n,1}^{ip}$, used for the second and third optimization objectives, are provided in equations 17–18 in table 3. Compared with the diffusion gain product, it requires one additional variable, the tortuosity factor anisotropy coefficient, $\tau^{tp/ip}$, defined in equation 8. Therefore, for a given baseline electrode and given tortuosity coefficients, the design parameters are R_V and $\tau^{tp/ip}$ for enforcing isotropic diffusion coefficient and R_V, $\tau^{tp/ip}$, and the width-to-thickness ratio of primary region noted R_t for enforcing isotropic characteristic diffusion time (cf. eq. 12a):

$$R_t = \frac{w_1}{L} \qquad [20]$$

Because the third optimization objective takes into consideration the largest set of parameters, design recommendations obtained through it are more relevant compared with the other two, even though it does not provide insight into how much a metric has been modified compared with the baseline electrode. Therefore, the recommended use of this model is to first determine the optimal ${R_V}^*$ value using the third optimization objective (i.e., $t_{tot}^{tp}/t_1^{ip}\,({R_V}^*) = 1$), then evaluating the diffusion gain product with this particular value $D_{tot,g}^{tp} \times D_{1,g}^{ip}({R_V}^*)$ as it quantifies the overall diffusion gain or loss compared with the baseline electrode. For example, a diffusion gain product less than one would indicate that to achieve diffusion time isotropy, the in-plane diffusion has been significantly degraded. Inversely, a diffusion gain product greater than one would indicate both optimization functions are compatible, implying this set of parameters is very promising. Another approach consists of considering an SPN for the parameter regions associated with the highest overall diffusion gain because it corresponds to the region where the SPN provides the most benefits.

Lastly, a fourth design parameter is considered for the bilayer case, the primary region thickness ratio noted R_L (cf. eq. 21). The unilayer case corresponds to $R_L = 1$. Adjusting the characteristic through-plane diffusion distance with $L + L_{III}$, the condition to enforce the isotropic diffusion time is modified as depicted in equation 12b.

$$R_L = \frac{L}{L + L_{III}} \quad [21]$$

$$\frac{t_{tot}^{tp}}{t_1^{ip}} = 1 \;\Rightarrow \frac{D_{tot}^{tp}}{D_1^{ip}} = \frac{D_{n,tot}^{tp}}{D_{n,1}^{ip}} = \frac{4 \times (L + L_{III})^2}{{w_1}^2} \times \left[1 + \frac{2(1 - R_L)}{R_L} + \left(\frac{1 - R_L}{R_L}\right)^2\right] \quad [12b]$$

All four design parameters derived from the optimization objective functions are expressed in ratio, indicating the optimization problem is adimensional.

4. Results

The investigated case parameters are summarized in table 4, based on the independent variables identified in §3.4. Cases 1 and 4 correspond to a low tortuosity anisotropy graphite, SLC1506T. Cases 2, 3, and 5 correspond to a high tortuosity anisotropy graphite, A12. Tortuosity factor through-plane coefficients γ, α of cases 1, 2, 4, and 5 have been fitted to match measured electrochemical data obtained at high C-rate, while the tortuosity factor of case 3 is extracted from microstructure characterization considering the carbon-binder phase [27]. Tortuosity anisotropy, $\tau_{tp/ip}$, of cases 1–5 are derived from microstructure characterization, as similarly done in [27]. A12 graphite exhibits elongated flake-like particles which induce a high tortuosity factor anisotropy, ~2.47 [27], larger than SLC1506T graphite, ~1.44. Because particles are misaligned, through-plane ionic diffusion is hindered for the unstructured electrode. In cases 1–3, optimal design parameters are provided considering equal thickness $L + L_{III} = L_{base}$, while cases 4 and 5 consider equal porosity $\varepsilon_{E,1} = \varepsilon_{E,base}$ (cf. §3.2). These last two cases do not preserve the volumetric and gravimetric theoretical specific capacity and are then relegated to Appendix B. Cases 6–8 investigate hypothetical electrodes considering variable tortuosity parameters with a constant porosity $\varepsilon_{E,base}$. Cases 9–11 investigate hypothetical electrodes considering both variable porosity $\varepsilon_{E,base}$ and tortuosity parameters. All cases, 1–11, represent a unilayer structured electrode. Design recommendations are expressed with R_V as they do not depend on the channel geometry contrarily with R_w. Design recommendations expressed with the secondary-region-width to primary-region-width ratio R_w are available in Appendix A considering both rectangular and cylindrical channel geometries, for case 1 only. Recommendations in terms of R_w differ significantly between the two channel geometries (cf. Fig. A1–3). In addition, two more configurations are considered: a fully sintered freeze-cast electrode (in §4.3) and a bilayer structured electrode (cases 12 and 13, Appendix C). The bilayer case is relegated to the appendices because the model only bounds the optimal solution.

Table 4. Parameters list of the investigated cases.[1]Optimal values are searched within this range. [2]Top and bottom values correspond, respectively, to rectangular and cylindrical channel geometry. [3]Bilayer cases are treated in Appendix C. [4]Identical porosity cases are treated in Appendix B.

Case	Baseline electrode volume fractions			Tortuosity parameters					SPN design parameters				Comparison choice: identical…
	$\varepsilon_{E,base}$	$\varepsilon_{AM,base}$	$\varepsilon_{CBD,base}$ k	γ	α	a	b	$\tau^{tp/ip}$	R_V[1]	R_w[2]	R_t	R_L[3]	
1	0.25-0.4	0.75-0.6	0 0	1.42	1.7	0	1	1.443	0-0.4	0-2/3 0-2.5	0.01-2	1	thickness
2	0.25-	0.75-0.6	0	1.92	2	0	1	2.471	0-0.4	0-2/3	0.01-2	1	thickness

	0.4		0							0-2.5			
3	0.25-0.4	0.543-0.679	0.057-0.071 9.488%	1.6	2.3	-1.114	1.714	2.471	0-0.4	0-2/3 0-2.5	0.01-2	1	thickness
4	0.25-0.4	0.75-0.6	0 0	1.42	1.7	0	1	1.443	0-0.4	0-2/3 0-2.5	0.01-2	1	porosity[4]
5	0.25-0.4	0.75-0.6	0 0	1.92	2	0	1	2.471	0-0.4	0-2/3 0-2.5	0.01-2	1	porosity[4]
6	0.3	0.7	0	1	1.5-3	0	1	0.5-5	0-0.3	0-0.43 0-1.61	0.2	1	thickness
7	0.3	0.7	0	1	1.5-3	0	1	2	0-0.3	0-0.43 0-1.61	0.01-2	1	thickness
8	0.3	0.7	0	1	2.25	0	1	0.5-5	0-0.3	0-0.43 0-1.61	0.01-2	1	thickness
9	0.25-0.4	0.75-0.6	0 0	0.5-3	2.25	0	1	2	0-0.4	0-2/3 0-2.5	0.2	1	thickness
10	0.25-0.4	0.75-0.6	0 0	1	1.5-3	0	1	2	0-0.4	0-2/3 0-2.5	0.2	1	thickness
11	0.25-0.4	0.75-0.6	0 0	1	2.25	0	1	0.5-5	0-0.4	0-2/3 0-2.5	0.2	1	thickness
12	0.25-0.4	0.75-0.6	0 0	1.42	1.7	0	1	1.443	0-0.4	0-2/3 0-2.5	0.01-2	0.9	thickness
13	0.25-0.4	0.75-0.6	0 0	1.42	1.7	0	1	1.443	0-0.4	0-2/3 0-2.5	0.01-2	0.8	thickness

4.1 Design recommendations for actual electrodes

Figure 4 shows the electrolyte transport properties for the different baseline (unstructured) electrodes investigated of cases 1–5. Results for cases 1–3 are presented in this section, while results for cases 4 and 5 are presented in Appendix B.

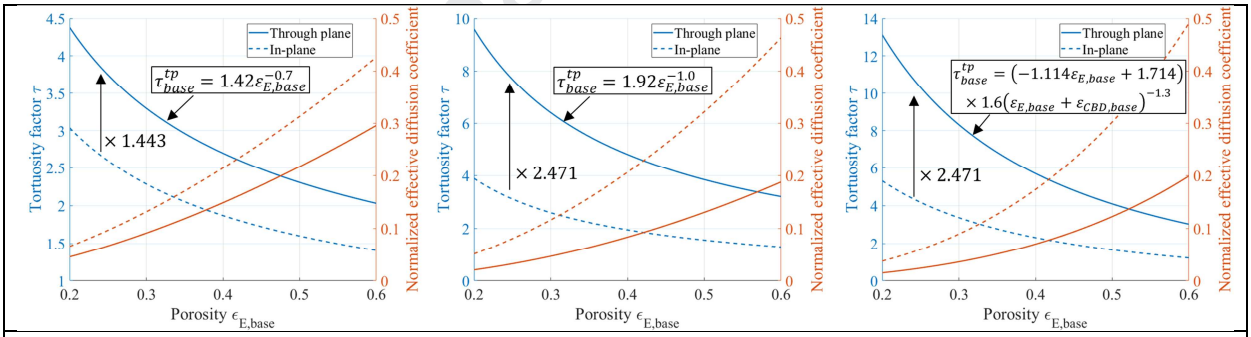

Figure 4. Baseline electrode electrolyte transport properties for: (left) low anisotropy electrode of cases 1 and 4, (middle) high anisotropy electrode of cases 2 and 5, and (right) high anisotropy electrode considering CBD of case 3.

Baseline and structured electrodes share the same thickness: $L = L_{base}$ then $\varepsilon_{E,1} < \varepsilon_{E,base}$. Figure 5 shows the primary region porosity of the structured electrode within the range of the investigated baseline electrode porosity. To keep the total porosity constant, increasing the SPN volume ratio or the region width ratio requires reducing the matrix porosity (primary region densification). Because the baseline and structured electrodes share the same CBD volume fraction ratio of active material volume fraction *k*, the porosity shown in figure 5 is independent of *k* (cf. eq. 13).

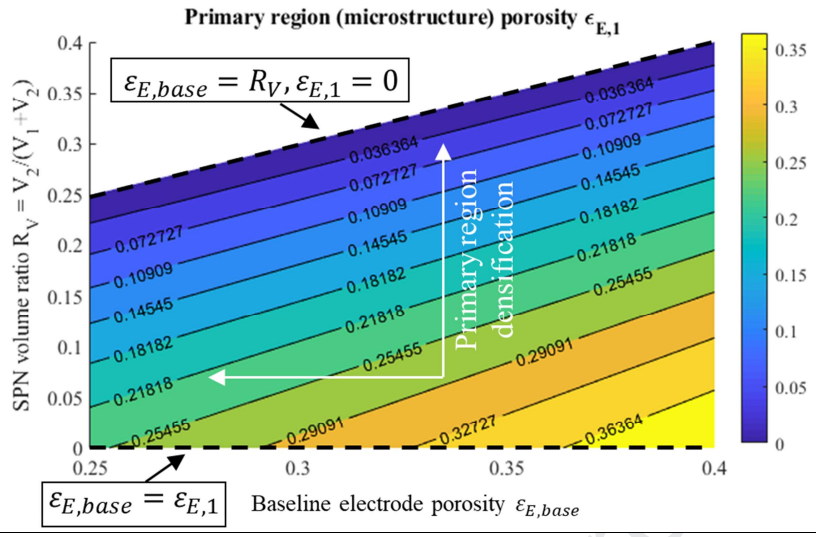

Figure 5. Primary region porosity as a function of the secondary region volume fraction and of the baseline electrode porosity. Empty map space corresponds to impossible design space (negative porosity).

Primary region in-plane normalized diffusion coefficient, $D_{n,1}^{ip}$, and structured electrode through-plane normalized diffusion coefficient, $D_{n,tot}^{tp}$, are shown in Figures 6a and 6b, respectively, for case 1. The SPN has a positive impact on $D_{n,tot}^{tp}$ but a negative impact on $D_{n,1}^{ip}$, while higher baseline electrode porosity, $\varepsilon_{E,base}$, enhances both diffusions. Diffusion improvement or degradation must be compared with the baseline unstructured electrode. Primary region in-plane diffusion gain, $D_{1,g}^{ip}$, and structured electrode through-plane diffusion gain, $D_{tot,g}^{tp}$, are then plotted, respectively, in figures 6c and 6d for case 1. The model predicts through-plane diffusion benefits more from the SPN for the small total porosity and the large SPN volume ratio, although such a preferred area corresponds to the worst degradation for the in-plane diffusion gain. This result clearly shows the ambivalent role of the SPN on diffusion. The SPN impact on the structured electrode through-plane tortuosity factor is quite significant (cf. Fig. 6e). For example, an SPN volume fraction of ~0.15 is enough to divide by two the initial tortuosity factor (from ~3.3 to ~1.65) for $\varepsilon_{E,base} = 0.3$. Eventually, the tortuosity factor is reduced to its theoretical limit 1 for the extreme case $R_V = \varepsilon_{E,base}$.

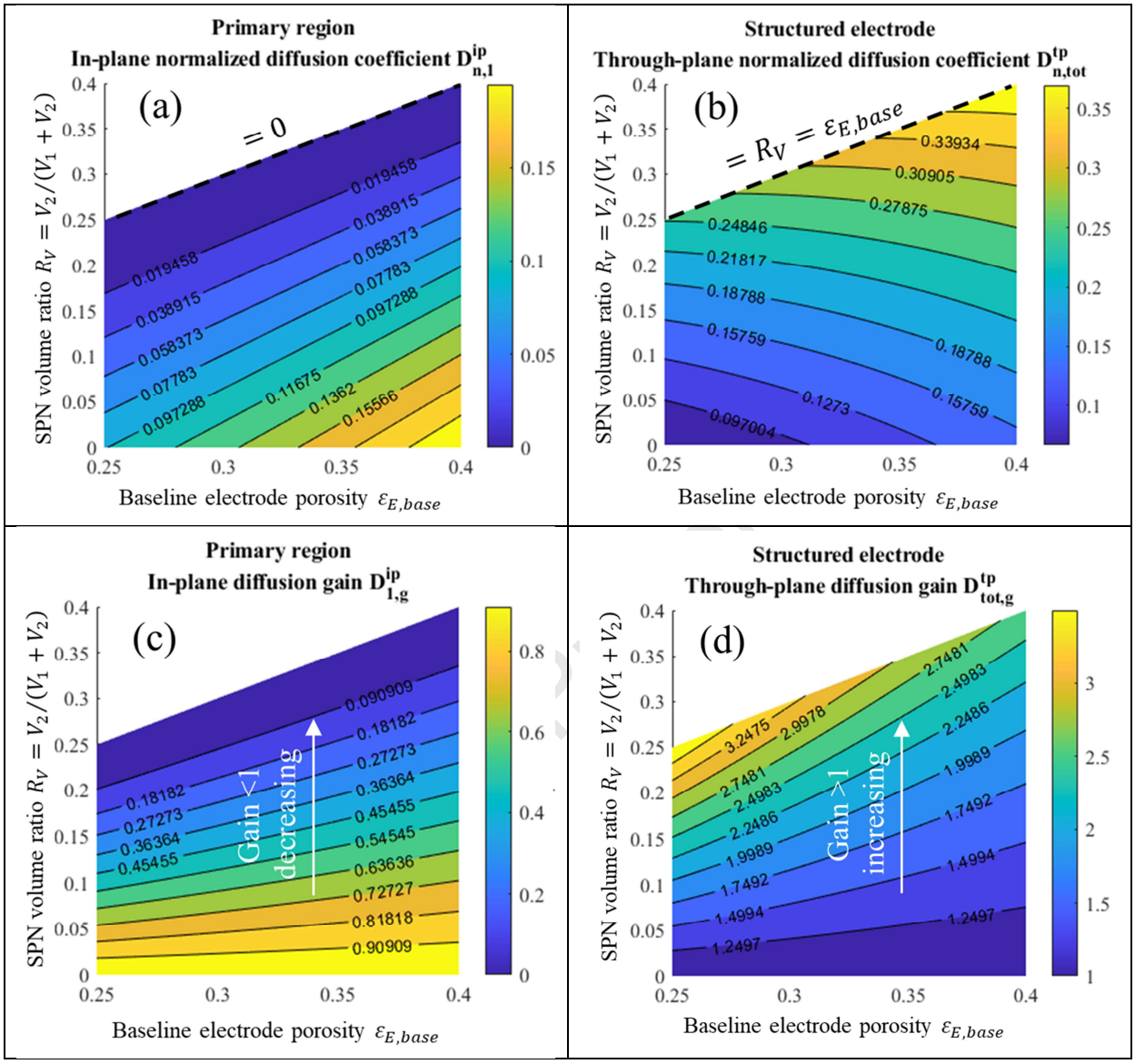
Primary region
In-plane normalized diffusion coefficient $D^{ip}_{n,l}$
(a)
$= 0$
SPN volume ratio $R_V = V_2/(V_1 + V_2)$
Baseline electrode porosity $\varepsilon_{E,base}$
Structured electrode
Through-plane normalized diffusion coefficient $D^{tp}_{n,tot}$
(b)
$= R_V = \varepsilon_{E,base}$
0.33934
0.30905
0.27875
0.24846
0.21817
0.18788
0.15759
0.1273
0.097004
Primary region
In-plane diffusion gain $D^{ip}_{l,g}$
(c)
Gain <1
decreasing
0.090909
0.18182
0.27273
0.36364
0.45455
0.54545
0.63636
0.72727
0.81818
0.90909
Structured electrode
Through-plane diffusion gain $D^{tp}_{tot,g}$
(d)
Gain >1
increasing
3.2475
2.9978
2.7481
2.4983
2.2486
1.9989
1.7492
1.4994
1.2497

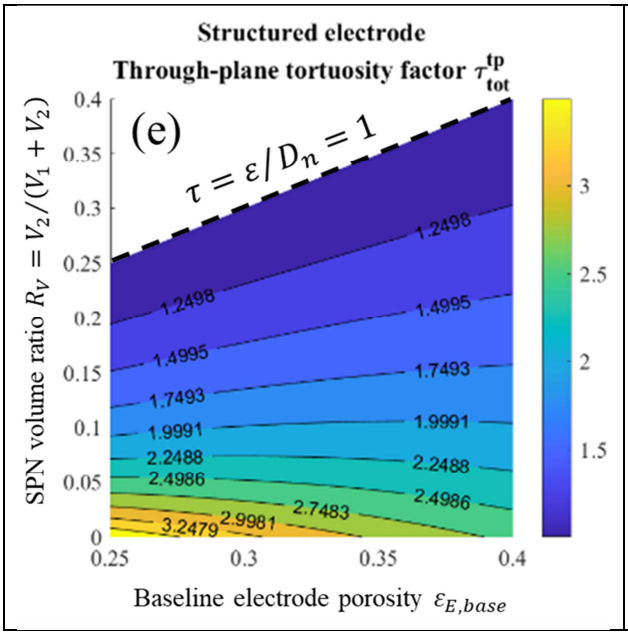

Figure 6. Case 1 ($\gamma = 1.42, \alpha = 1.7, \tau^{tp/ip} = 1.443$). Normalized diffusion coefficient of (a) in-plane primary region, $D_{n,1}^{ip}$, and (b) through-plane structured electrode, $D_{n,tot}^{tp}$. Diffusion gain for (a) in-plane primary region, $D_{1,g}^{ip}$, and (d) through-plane structured electrode, $D_{tot,g}^{tp}$. Through-plane structured electrode tortuosity factor, τ_{tot}^{tp}, is also shown (e).

Furthermore, for a given total porosity, the primary region in-plane diffusion loss rises faster with the SPN volume ratio than structured electrode through-plane diffusion gain (cf. Fig. 7). This is expected because the tortuosity factor changes with porosity according to a power law, with its derivative higher for the low porosity [27]. Therefore, primary region in-plane diffusion loss is growing exponentially with SPN volume ratio. On the contrary, structured electrode through-plane diffusion follows a rule of mixture (cf. eq. 6a) controlled by its second term, $1 \times V_2/(V_1 + V_2)$, equals to the SPN volume fraction R_V, as its first term $D_{n,1}^{tp} \times V_1/(V_1 + V_2)$ is vanishing quickly with R_V. As a consequence, structured electrode through-plane diffusion gain grows linearly with SPN volume ratio and cannot match the exponential loss rate of the primary region in-plane diffusion loss. This limits the maximum SPN volume ratio in terms of diffusion. The diffusion gain product increases with the SPN volume fraction R_V until it reaches a maximum because it becomes too detrimental to densify the primary region (cf. Fig. 7). This inflexion point is reached further for the second electrode (case 2) and is associated with a higher overall diffusion gain indicating more tortuous electrodes can achieve better diffusion (coefficient) trade-offs with SPN. Note that the difference in term of tortuosity anisotropy between cases 1 and 2 does not explain this result because the diffusion gain product is not a function of $\tau^{tp/ip}$ (cf. eq. 15–16).

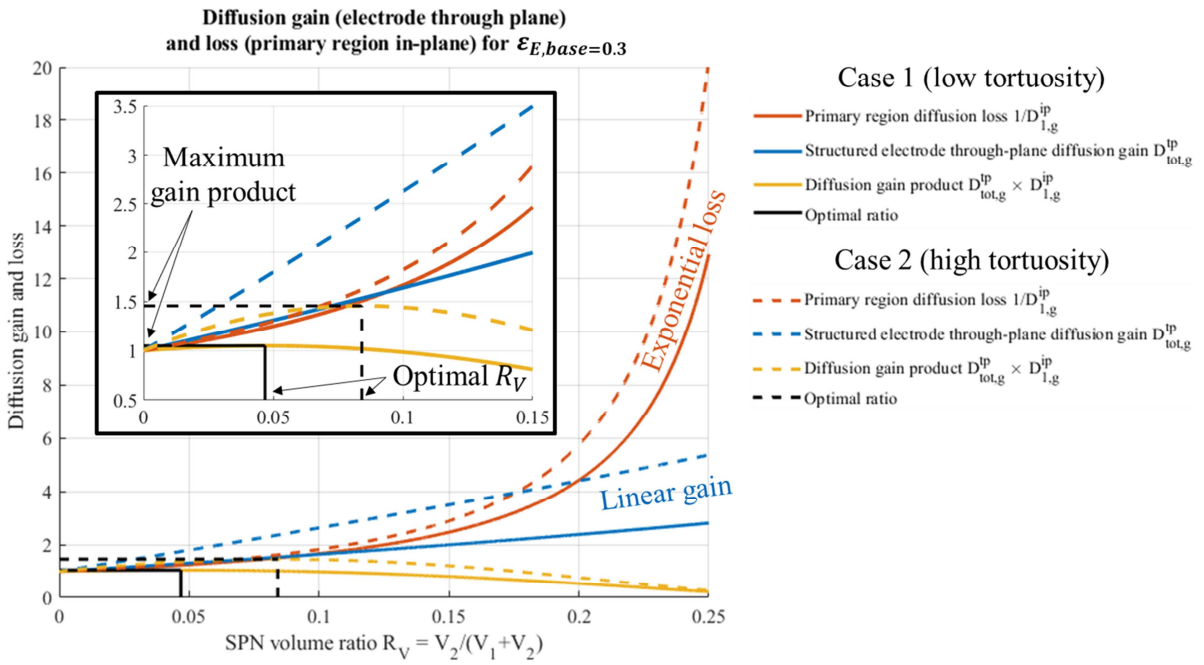

Figure 7. Through-plane diffusion gain $D^{tp}_{tot,g}$ and primary region in-plane diffusion loss $1/D^{ip}_{1,g}$ plotted as a function of the SPN volume fraction R_V for a constant total porosity 0.3, for case 1 (solid lines) and 2 (dashed lines) electrodes.

Results of the first optimization objective, maximizing diffusion gain product, are shown in figure 8 for cases 1–3 for all of the baseline electrode porosities investigated. Because of the limitation discussed in the previous paragraph, only relatively low SPN volume ratios are recommended: 4.7 (3.9)%, 8.4 (10.6)%, and 9.0 (10.4)%, associated with a diffusion gain product of 1.05 (1.01), 1.46 (1.27), and 1.71 (1.31), respectively, for cases 1, 2, and 3 for $\varepsilon_{E,base}$ equals to 0.3 (0.4). While the product diffusion gain may be quite limited, it actually corresponds to a significant through-plane diffusion gain (e.g., 1.29 for case 1 with $\varepsilon_{E,base}$ equals 0.3 (cf. Fig. 7)). The maximum gain is centered on the low porosity, high tortuosity regions, confirming that more tortuous electrodes can achieve better diffusion trade-offs with an SPN. Furthermore, a larger design space is recommended ($D^{tp}_{tot,g} \times D^{ip}_{1,g} > 1$) for cases 2 and 3, indicating highly tortuous electrodes not only benefit more from an SPN but are also less restricted with the SPN volume fraction choice.

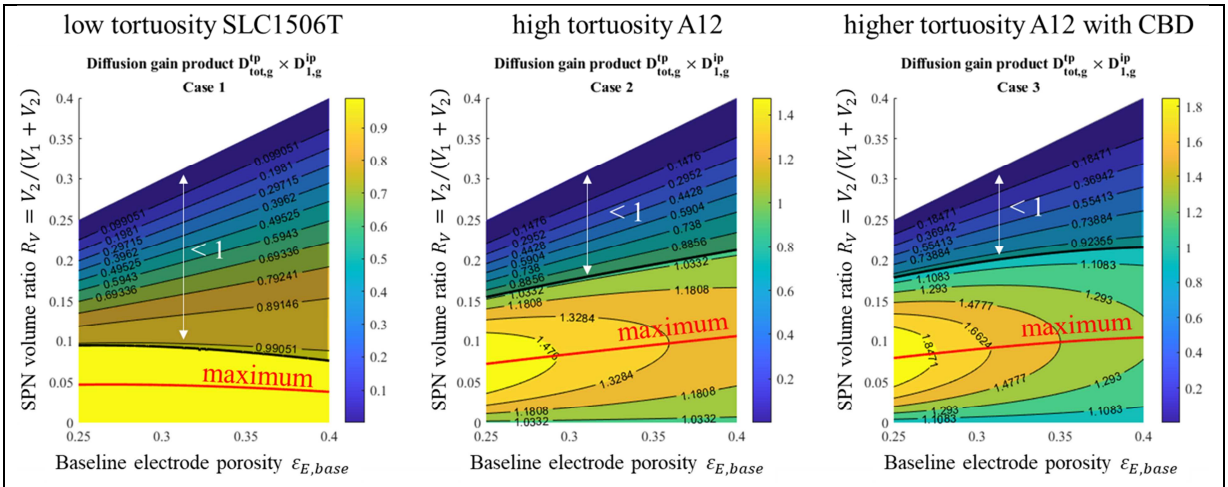

Figure 8. Diffusion gain product map as a function of baseline electrode porosity, $\varepsilon_{E,base}$, and the secondary pore network volume fraction R_V for (left) case 1, (middle) case 2, and (right) case 3 electrodes. Unit isoline is black line and the optimal R_V that maximizes diffusion gain product is red line (first optimization objective). The transparent grey area corresponds to a diffusion gain product below 1, thus an overall loss region to avoid. Results are independent from tortuosity anisotropy $\tau^{tp/ip}$.

Optimal SPN volume fractions R_V that fulfill the second (enforcing isotropic diffusion coefficient) and third (enforcing isotropic characteristic diffusion time) optimization objectives are shown in figure 9. Low SPN volume fraction corresponds to through-plane diffusion limitation, while high SPN volume fraction corresponds to in-plane diffusion limitation. To achieve isotropic diffusion coefficient, relatively low R_V values are required (cf. Fig. 9 left column). However, to achieve isotropic diffusion time, significantly larger SPN volume ratios are recommended compared with the two other optimization objectives (cf. Fig. 9, right column). Indeed, for low width-to-thickness ratios of the primary region R_t, higher SPN volume ratio are recommended because thicker electrodes benefit more from straight channels all along the electrode thickness. The extreme case $R_t \to 0$ (electrode infinitely thick compared with primary region width, $w_1/L \to +\infty$) corresponds to $D^{tp}_{n,tot}/D^{ip}_{n,1} \to +\infty$ (cf. eq. 12a). Considering equation 17b, knowing that γ and $\tau^{tp/ip}$ are nonzero terms by definition, and because $(\varepsilon_{E,base} - 1)/(1 - R_V) + 1$ ranges from 0 to $\varepsilon_{E,base}$, respectively, for $R_V = \varepsilon_{E,base}$ and $R_V = 0$, it implies $R_t \to 0$ occurs only for $R_V \to \varepsilon_{E,base}$ as $(0 + \delta)^{-\alpha} \to +\infty$. Then, for the extreme case, $R_t \to 0$, the recommended SPN design parameter for structured electrode with $w_1 \ll L$ is $R_V = \varepsilon_{E,base}$, which corresponds to the extreme case of a fully dense primary region (e.g., from sintering) associated with an ultra-thick electrode (e.g., from freeze-casting). Inversely, for high R_t, a low SPN volume ratio is recommended as through-plane diffusion time is sufficiently low compared to in-plane diffusion time. Eventually, for very high R_t value (close to 2.5), an optimal R_V does not exist.

For a given thickness-width ratio, the recommended SPN volume ratio increases with the total porosity $\varepsilon_{E,base}$ (cf. Fig. 9), because the detrimental impact of the primary region in-plane diffusion time decreases. This is derived from the tortuosity-porosity power law (cf. eq. 2): $d\tau/d\varepsilon = \gamma(1 - \alpha)\varepsilon^{-\alpha}$

decreases with ε: at high porosity, reducing the porosity in the primary region due to an increase of R_V has a limited impact on tortuosity. However, higher porosity also reduces the through-plane diffusion gain (cf. Fig. 6) and product diffusion gain (cf. Fig. 8), indicating the SPN benefit is less strong. For example, for $R_t = 0.2$, the optimal SPN volume ratio at $\varepsilon_{E,base} = 0.25$ is 22.9% according to the third optimization objective for case 1 (cf. Fig. 9), which corresponds to a through-plane diffusion gain of 3.45 (cf. Fig. 6d) and to a product diffusion gain of 0.08 (cf. Fig. 8). For $\varepsilon_{E,base} = 0.4$, the optimal SPN ratio is 37.6%, which corresponds to a reduced through-plane diffusion gain and product diffusion gain of 2.55 and 0.05, respectively. This result illustrates that, while the optimum is deduced from the diffusion time isotropy constraint, the magnitude of the improvement is provided by the diffusion gain analysis. Also, the optimum does not necessarily correspond to the region $D_{tot,g}^{tp} \times D_{1,g}^{ip} > 1$. Relatively similar recommendations are provided for both electrodes (cf. Fig. 9), although with higher associated diffusion gains for cases 2 and 3 (cf. Fig. 8). Since both second and third optimization functions depend on the through-plane tortuosity coefficients α, γ, but also on the tortuosity factor anisotropy $\tau^{tp/ip}$, and that cases 1, 2, and 3 have different α, γ and $\tau^{tp/ip}$ parameters, deconvoluting their respective impact on the choice of the optimal R_V is not straightforward. Such a detailed analysis is performed in section §4.2.

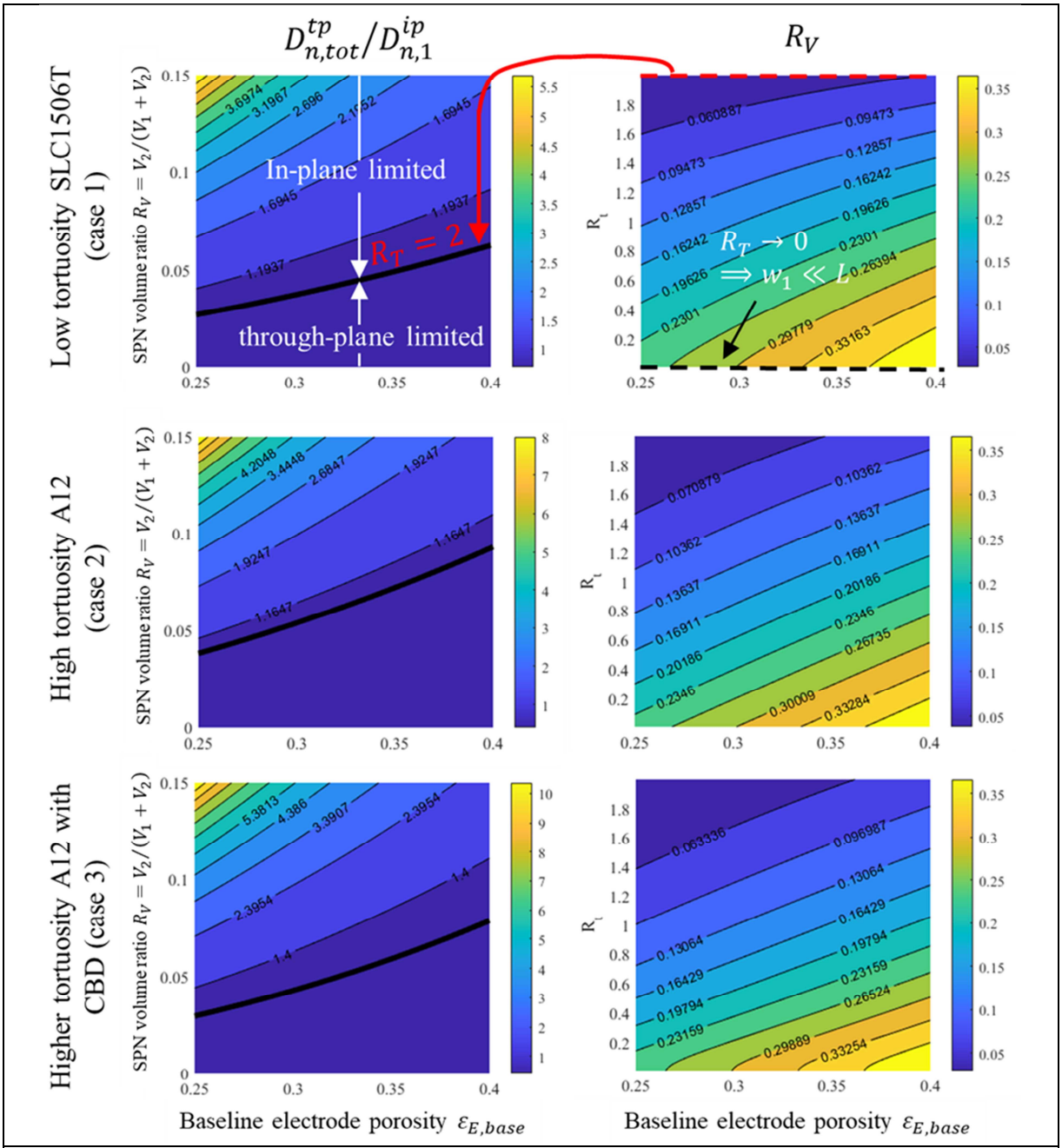

Figure 9. Optimal SPN volume fraction R_V considering (left) second optimization objective, enforce isotropic diffusion coefficient, with thick line being the optimal values and (right) third optimization objective, enforce isotropic characteristic diffusion time, with 2D map being the optimal values. Left column corresponds to the specific case $R_t = 2$ of the third optimization objective (red dashed line). (Top) case 1, (middle) case 2, and (bottom) case 3 electrodes. Results are dependent on tortuosity anisotropy $\tau^{tp/ip}$.

Table 5 summarizes design recommendations and impacts on transport for a limited number of porosities and width-to-thickness ratios. As discussed in §3.4, the most relevant optimization function is

the third one (isotropic diffusion time); therefore, only its design recommendations are listed in table 5. For the same porosity and width-to-thickness ratio, all cases share relatively similar optimal R_V values, with a maximal R_V difference of 0.37. The impact of different tortuosity coefficients on the choice of the optimal SPN design parameter is explored in more detail in §4.2.

Table 5. Design parameter recommendation.[1]Optimal SPN volume fraction R_V deduced from third optimization objective. Structured electrode through-plane diffusion gain, $D_{tot,g}^{tp}$, structured electrode through-plane tortuosity factor, τ_{tot}^{tp}, and diffusion product gain, $D_{tot,g}^{tp} \times D_{1,g}^{ip}$, values are given for this optimal R_V. [2] Unstructured baseline tortuosity factor → structured tortuosity factor.

$\varepsilon_{E,base}$	R_t	**Case 1** *Low through-plan tortuosity, low tortuosity anisotropy*			**Case 2** *High through-plan tortuosity, high tortuosity anisotropy*			**Case 3** *High through-plan tortuosity, high tortuosity anisotropy, with CBD*		
		Optimal[1] R_V	$D_{tot,g}^{tp}$ $\tau_{tot}^{tp\ 2}$	$D_{tot,g}^{tp} \times D_{1,g}^{ip}$	**Optimal[1] R_V**	$D_{tot,g}^{tp}$ $\tau_{tot}^{tp\ 2}$	$D_{tot,g}^{tp} \times D_{1,g}^{ip}$	**Optimal[1] R_V**	$D_{tot,g}^{tp}$ $\tau_{tot}^{tp\ 2}$	$D_{tot,g}^{tp} \times D_{1,g}^{ip}$
0.3	1	16.3%	2.08 3.29→1.58	0.75	14.9%	3.46 6.40→1.85	1.22	13.1%	3.97 8.31→2.09	1.59
	0.2	27.8%	3.05 3.29→1.08	0.06	26.6%	5.70 6.40→1.12	0.13	26.9%	7.44 8.31→1.12	0.22
0.4	1	24.4%	1.88 2.69→1.43	0.61	23.0%	3.00 4.80→1.60	0.91	20.7%	3.21 5.70→1.78	1.05
	0.2	37.7%	2.54 2.69→1.06	0.05	36.6%	4.41 4.80→1.09	0.08	36.7%	5.27 5.70→1.08	0.10

4.2 Design recommendations for hypothetical electrodes

Figure 10 shows the electrolyte transport properties for the different baseline (unstructured) electrodes investigated in cases 6–11. Compared with cases 1–5 where tortuosity coefficients were fixed, then associated with a given microstructure, all cases 6–11 investigate variable tortuosity coefficients, thus sweeping a large microstructure design space. All cases are compared with constant thicknesses and without carbon binder.

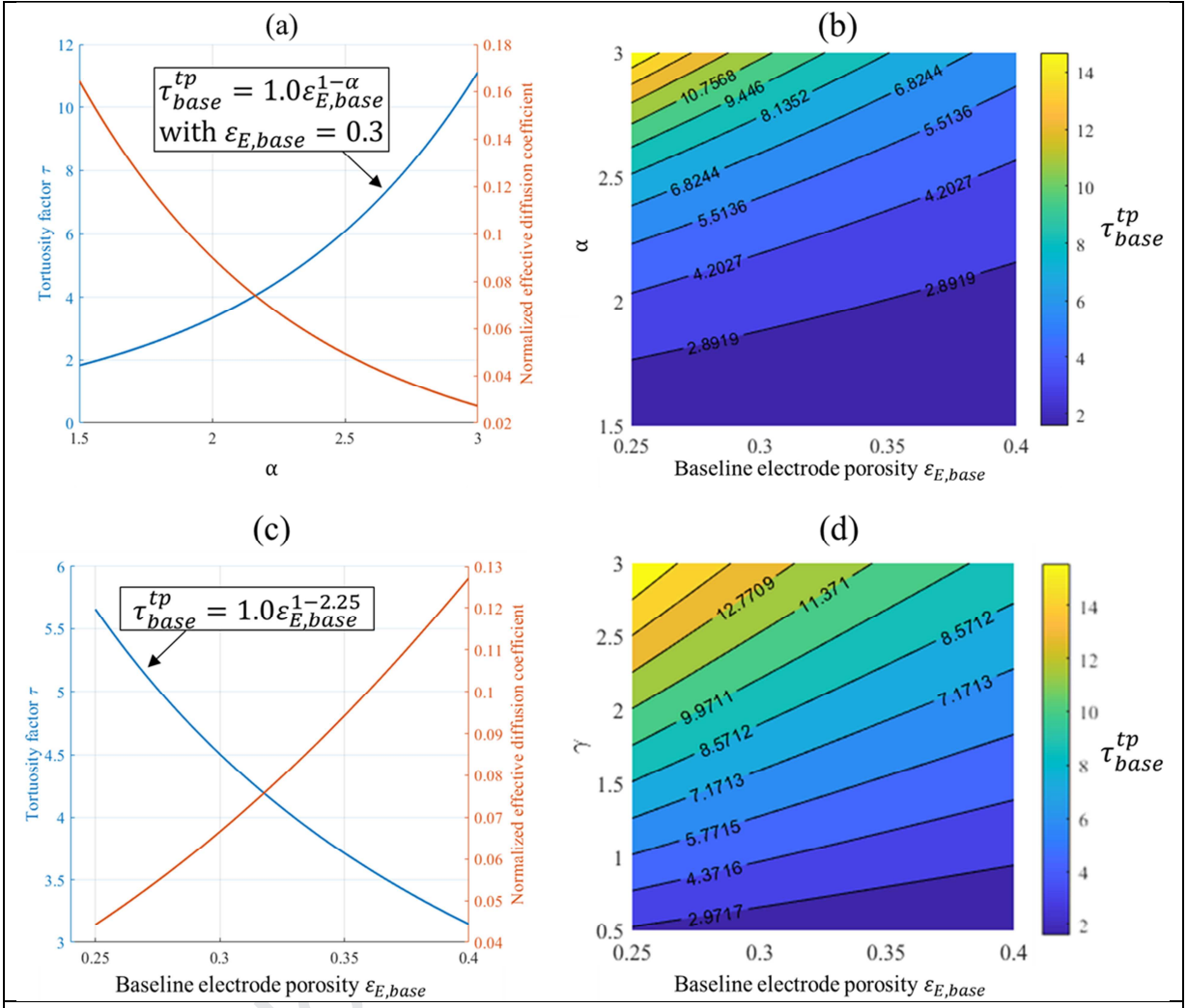

Figure 10. Baseline electrode electrolyte through-plane transport properties of (a) cases 6–8 considering a unique porosity, for the case 8, $\propto = 2.25$, (b) case 9, (c) case 10, and (d) case 11. Only through-plane transport is showed.

4.2.1 Variable tortuosity parameters, unique baseline electrode porosity

Case 6 investigates variable $\propto, \tau^{tp/ip}$, case 7 investigates variable $\propto, R_t$, and case 8 investigates variable $\tau^{tp/ip}, R_t$ considering a unique electrode baseline porosity $\varepsilon_{E,base}$. Diffusion gain analysis reveals nothing new for case 8 because it does not depend on tortuosity anisotropy. Although cases 6 and 7 provide two messages (cf. Fig. 11). First, for electrodes with low-enough tortuosity, there is no or limited gain to be expected from SPN in terms of overall diffusion improvement, while the gain increases with α. Second, recommended R_V reaches a maximum for high tortuosity coefficient α, indicating that SPN design R_V is capped for a given baseline electrode porosity. Note that it is not an asymptotic behavior because, for extremely high tortuosity coefficients (that are not relevant for realistic microstructures), this value decreases (cf. Fig. 11 insert).

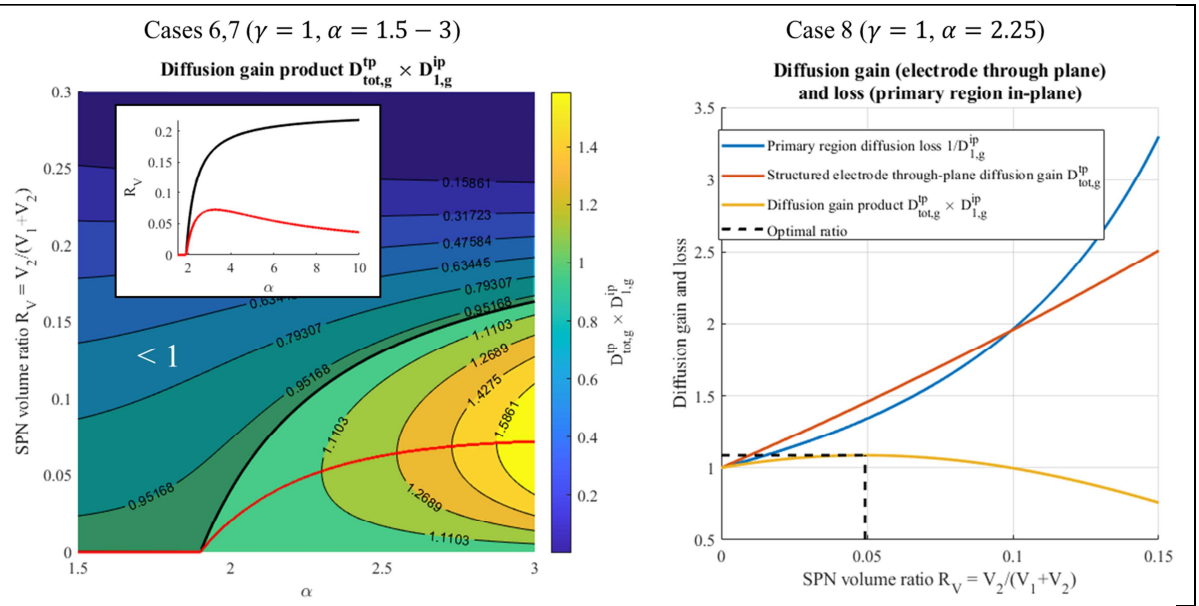

Figure 11. (Left) Diffusion gain product map as a function of the tortuosity coefficient α and the SPN volume fraction R_V for cases 6 and 7. Unit isoline is the black line and optimal R_V that maximizes diffusion gain product is the red line (first optimization objective). Transparent grey area corresponds to a diffusion gain product below 1, thus an overall loss region to avoid. Insert shows the recommended values for very high values of α. (Right) Diffusion gain product plotted as a function of the SPN volume fraction R_V for case 8.

Considering second and third optimization objectives, several messages can be extracted (cf. Fig. 12). First, the SPN volume fraction R_V is limited by high tortuosity coefficient α, because any primary region densification induces a sharp increase of tortuosity factor within the primary region (cf. Fig. 12a-d), even though this restriction can be mitigated for anisotropic electrode for which in-plane diffusion is better than through-plane (i.e., $\tau^{tp/ip} > 1$). This combination, high through-plane tortuosity coefficient $\propto$ and high tortuosity anisotropy $\tau^{tp/ip}$, then fits the SPN architecture particularly well because it benefits from a large diffusion gain (from $\propto$, cf. Fig. 11), while still have access to a wide choice of R_V due to $\tau^{tp/ip}$ (cf. Fig. 12a, b, e, f). Electrodes with elongated particles misaligned with the diffusing path (i.e., long diameter perpendicular with it), for instance some graphite materials [22, 27], are then a relevant application for SPN: channels improve the through-plane diffusion while flake-like particles enhance the in-plane diffusion within the primary region. Second, to achieve isotropic diffusion time, significantly larger SPN volume ratios are recommended compared with the two other optimization objectives, especially for low width-to-thickness ratios of the primary region R_t (cf. Fig. 12d, f). Indeed, as discussed in §4.1, R_V tends toward $\varepsilon_{E,base}$ when R_t is near 0 ($L \gg w_1$). Third, as R_t increases, the weights of $\propto$ and $\tau^{tp/ip}$ in the choice of R_V increase, while these two parameters are negligible for very low R_t (cf. Fig. 12d, f).

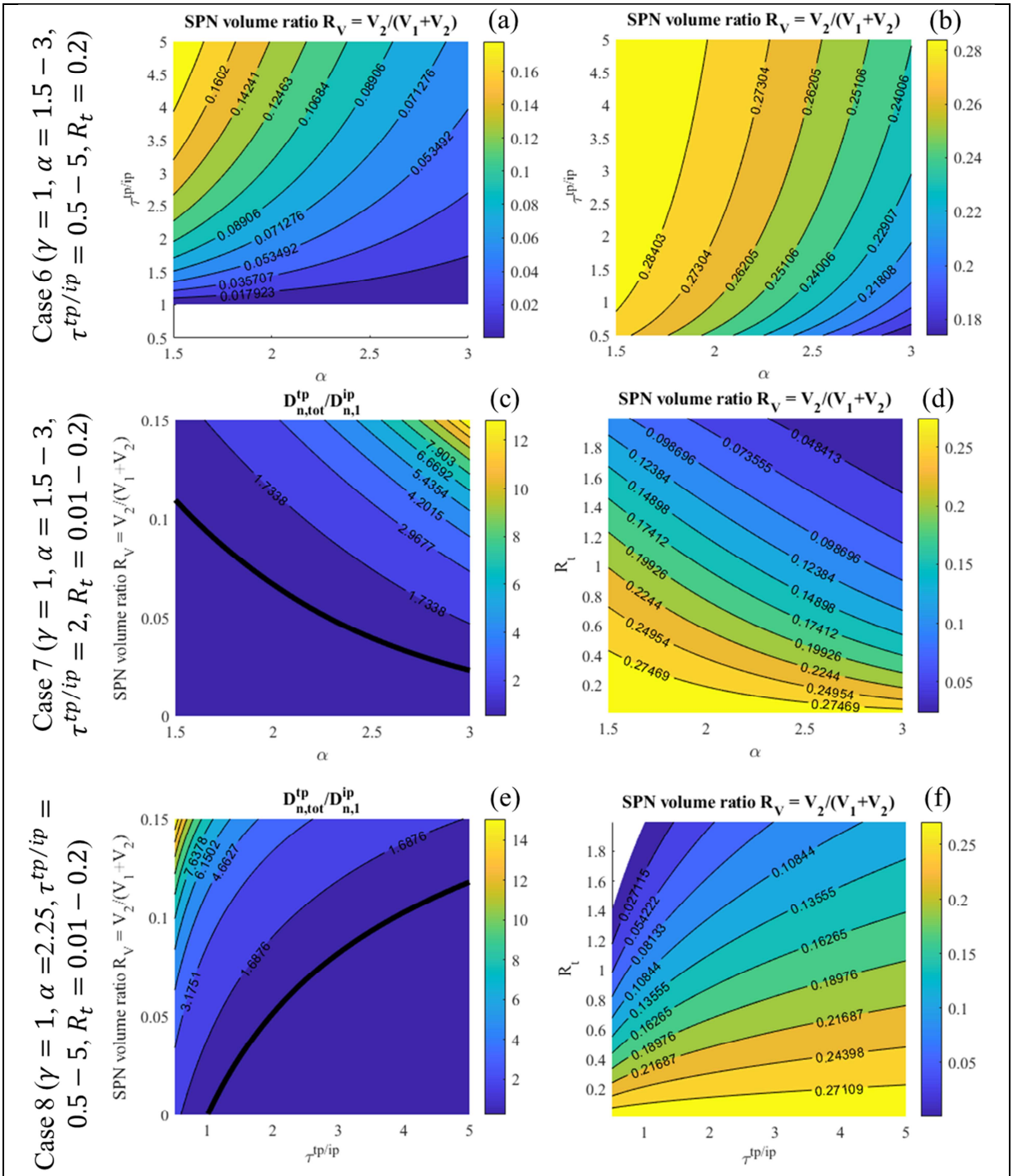

Figure 12. Optimal SPN considering (left) second optimization objective, enforce isotropic diffusion coefficient and (right) third optimization objective, enforce isotropic characteristic diffusion time. Optimal SPN volume fraction R_V is (c, e) thick line and (a, b, d, f) 2D map. (a, b) case 6, (c, d) case 7, and (e, f) case 8.

4.2.2 Variable tortuosity parameters and baseline electrode porosity

Case 9 investigates variable $\varepsilon_{E,base}$, γ , case 10 investigates variable $\varepsilon_{E,base}$, $\propto$ and case 11 investigates variable $\varepsilon_{E,base}$, $\tau^{tp/ip}$ considering a unique width-to-thickness ratio of primary region $R_t = 0.2$. Diffusion gain analysis reveals nothing new for case 11 because it does not depend on tortuosity anisotropy. Although cases 9 and 11 provide two messages (cf. Fig. 13). First, both $\propto$ and γ have similar trends on the overall diffusion gain and on the choice of R_V. Higher gains are achieved for low-porosity, high-tortuosity coefficients (i.e., high-tortuosity factor region). Second, as said before (cf. §4.2.1, Fig. 11), there is little benefit to use an SPN for low-tortuosity coefficient values, even though an SPN can be beneficial for lower values of γ and $\propto$ as electrode porosity is reduced (cf. Fig. 13 a, c).

Figure 14 shows the optimal SPN R_V for cases 9–11. Higher tortuosity coefficients α, γ reduce the optimal value of R_V, while higher tortuosity anisotropy $\tau^{tp/ip}$ increases it. This result indicates the trend already discussed in figure 12 is valid for all the porosity investigated. The coefficients α, γ, and $\tau^{tp/ip}$ have a lower weight on the choice of R_V for the third optimization objective (cf. Fig. 14, right column) compared with the second optimization objective (cf. Fig. 14, left column). Enforcing $D_{tot}^{tp}/D_1^{ip} = 1$ (second optimization objective) is a particular case of $t_{tot}^{tp}/t_1^{ip} = 1$ (third optimization objective) with $4 \times L^2/{w_1}^2 = 1$ (cf. eq. 12a), i.e. $R_t = 2$. Such high values of R_t are associated with significant dependences of R_V on α and $\tau^{tp/ip}$ (cf. Fig. 12). Contrarily, a low value of R_t 0.02 used for cases 9–11 corresponds to a low sensitivity region (cf. Fig. 12), because R_V tends toward $\varepsilon_{E,base}$ when R_t is near 0.

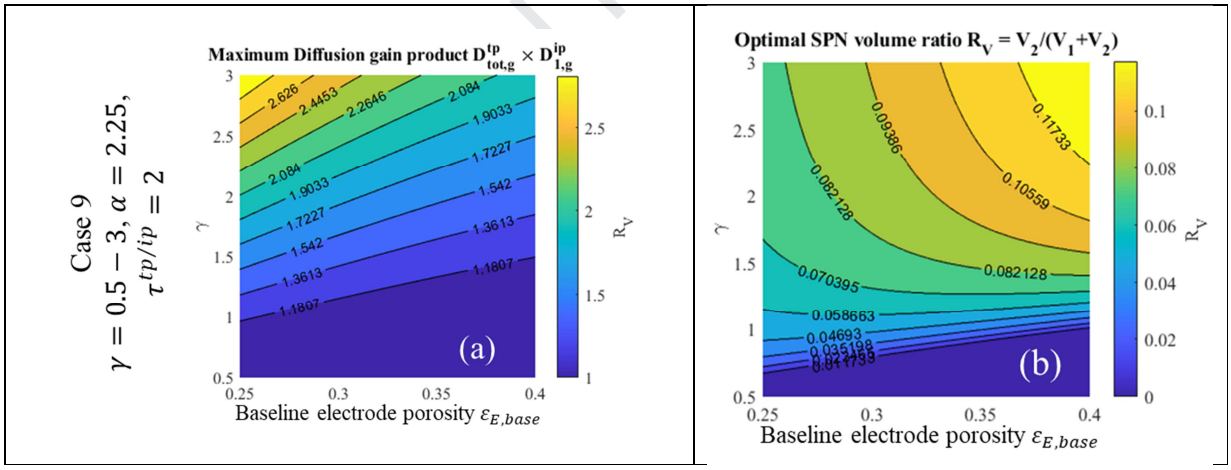

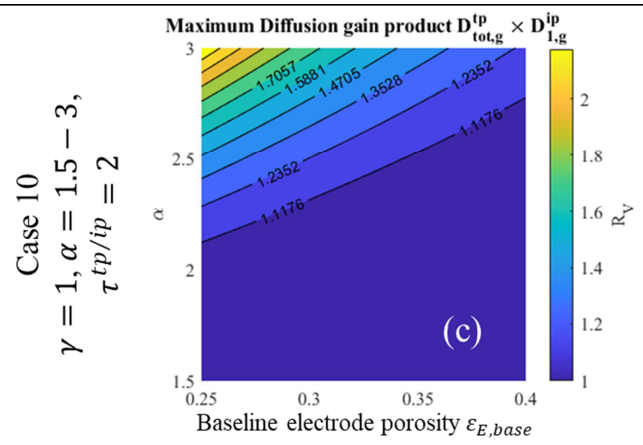

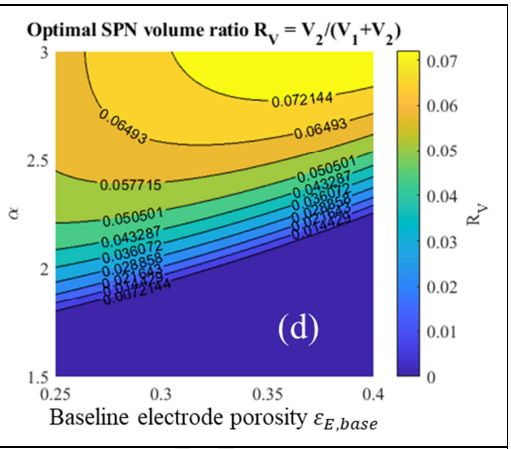

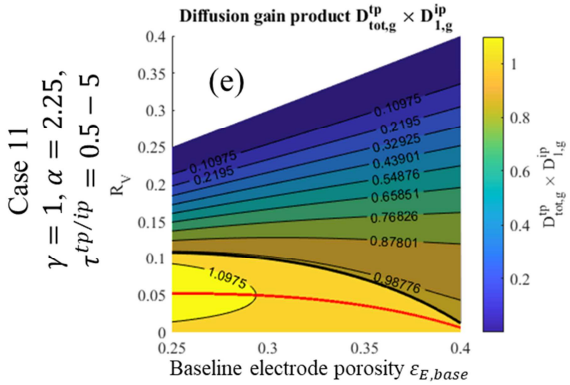

Figure 13. (a, b) Case 9 and (c, d) case 10 with (left) the maximum diffusion gain product achievable and (right) the associated optimal SPN volume fraction R_V that provides this maximum. (e) Case 11, diffusion gain product map. Unit isoline is the black line and the optimal R_V that maximizes diffusion gain product is the red line. The transparent grey area corresponds to a diffusion gain product below 1; thus, an overall loss region to avoid.

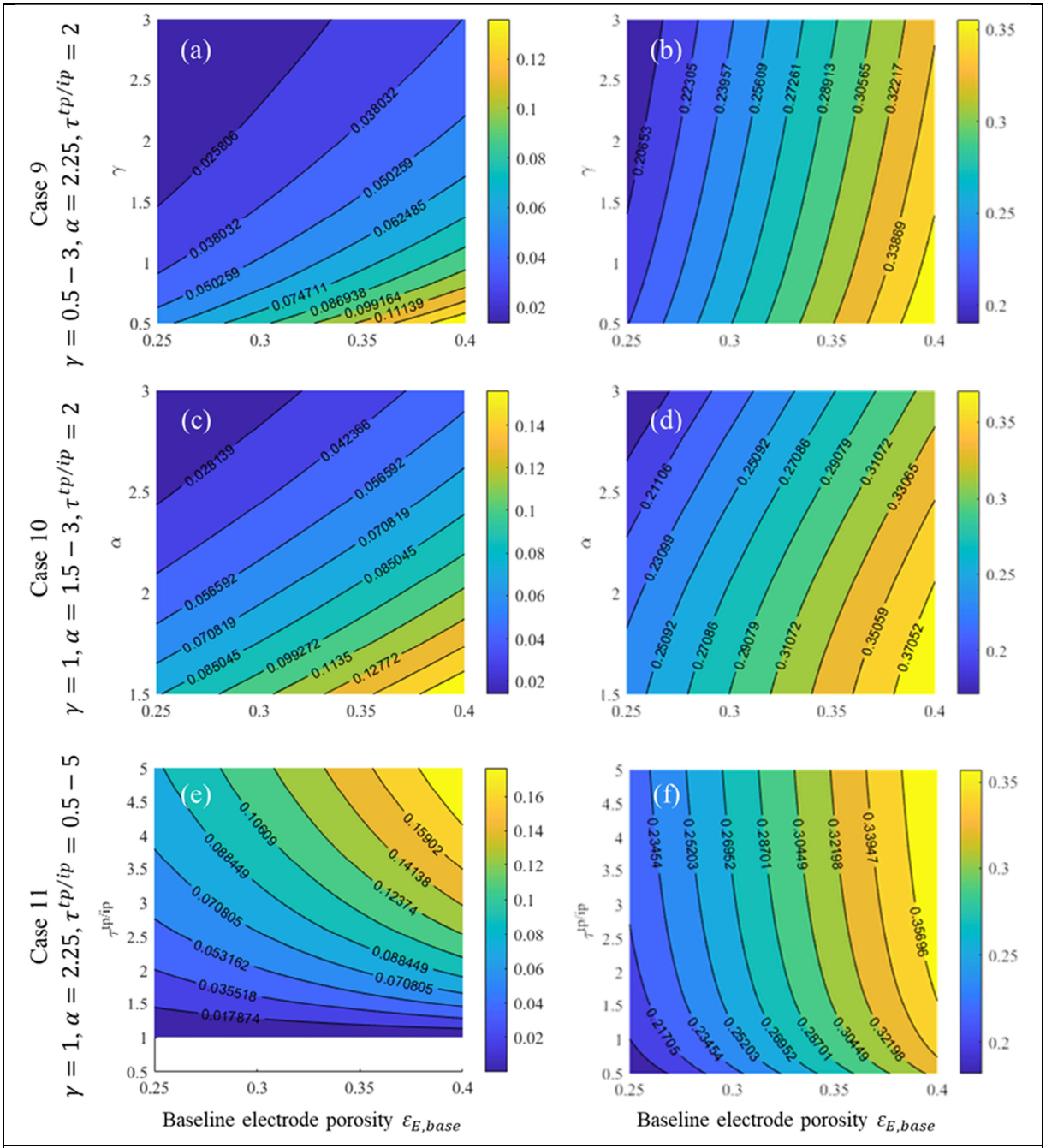

Figure 14. Optimal SPN 2D map considering (left) second optimization objective, enforce isotropic diffusion coefficient and (right) third optimization objective, enforce isotropic characteristic diffusion time. (a, b) Case 9, (c, d) case 10, and (e, f) case 11.

4.3 Fully dense primary region

The last case investigates a fully dense primary region. This extreme case corresponds to a freeze- cast electrode for which a post-processing sintering step leads to maximum densification

of the active material. In such cases, there is not ionic diffusion within the primary region, and the active electrochemical interface is only at the interface primary secondary region. An SPN will still improve the ionic through-plane diffusion, but will hinder the in-plane solid-state diffusion, as reported by [13]. The in-plane diffusion characteristic time is ${w_1}^2/4D_s$, while the through-plane diffusion characteristic time is L^2/D_{tot}^{tp}, with D_2^{tp} the electrolyte diffusion coefficient D_e. For a given w_1 and L, the secondary region width w_2 is deduced so that diffusion time is isotropic. Figure 15 shows the results for two different electrode materials. The region for which a solution exists is bounded by electrolyte through-plane transport limitation (large thickness and small primary region width region), and by solid-state in-plane transport limitation (small thickness and large primary region width region). For an electrode with lower solid-state diffusion coefficient, this region is displaced toward the large thickness and small primary region width region (cf. Fig. 15c). This result indicates freeze-casted process followed by a post-sintering step is more relevant for ultra-thick electrodes with a moderate primary region width.

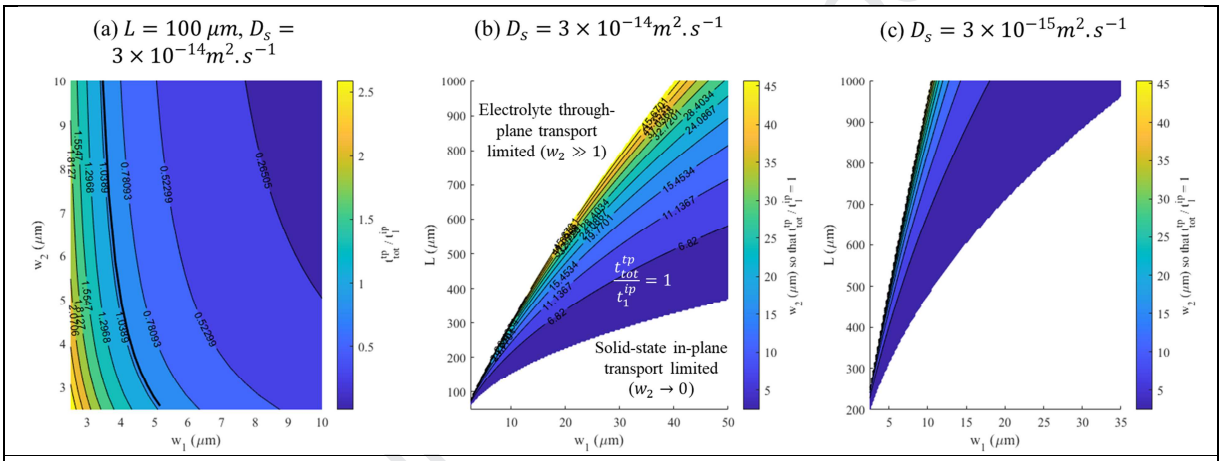

Figure 15. Design recommendation for freeze-casting sintered case (fully dense primary region). (a) Considering a constant electrode thickness $L = 100$ µm, 2D map is the characteristic diffusion time ratio between electrode through-plane (liquid state) and primary region in-plane (solid state), thick line is the optimal doublet w_1, w_2 that correspond to unit ratio. (b, c) Considering a variable electrode thickness, 2D map is the channel width w_2 that corresponds to a unit ratio. White space corresponds to no solution considering the investigated w_2 range (2.5–50 µm). (a, b) corresponds to a graphite electrode ($D_s = 3 \times 10^{-14} m^2.s^{-1}$), while (c) corresponds to an NMC electrode ($D_s = 3 \times 10^{-15} m^2.s^{-1}$). Both cases are using an electrolyte diffusion coefficient of $D_e = 1.35 \times 10^{-10} m^2.s^{-1}$.

5. Tortuosity factor requirement to enable fast charging of thick electrodes

A macro-homogeneous pseudo-2D model used in the previous works [1,40] is employed to initially investigate the effect of tortuosity factor on extreme fast charge behavior for a graphite/NMC 532 cell with a loading of 3 mAh.cm-2, 35% porous electrodes, operating at 45°C. Figure 16 illustrates how the usable discharge energy density and potential for lithium plating changes as a function of

charge rate for constant current (CC) only charging up to 4.2 V and considering three different tortuosity factors, τ^{tp}. First, a relatively high value, 3.2, representative of measured tortuosity factors for electrodes fabricated with conventional fabrication techniques using relatively spherical particles for both electrodes and the binder phase [27]. Second, an intermediate value, 1.5, deduced from the analytical transport model discussed above using case 1 (corresponds to roughly spherical particles) with $\varepsilon_{E,base} = 0.35$ and $R_t = 1$, which corresponds to an optimal $R_V = 0.2$ (considering the third optimization objective, cf. Fig. 9) with an improved through-plane tortuosity down from 3.0 to 1.5 (cf. Fig. 6e). Lastly, results are illustrated for an electrode with a tortuosity factor of 1 representing the theoretical limit for any novel electrode design. The potential for lithium plating is the potential of the solid phase anode minus that of the electrolyte phase at the graphite/separator interface. When this value approaches or drops below zero, plating is expected.

Figure 16 highlights that improving the tortuosity for moderate loading cells can significantly improve the high rate charging performance and mitigate lithium plating. For a conventional electrode cell, the achievable energy density is only around 200 Wh/L at 6C compared to a total cell energy density of 600 Wh/L. Reducing the tortuosity factor to 1.5 would enable a 6C energy density of roughly 335 Wh/L, or 55% state of charge change. Further, the conventional electrode cell is expected to plate lithium at rates >4C. Reducing the tortuosity factor is predicted to enable 6C charging without lithium plating. These results provide motivation for further investigation into methods for reducing the through-plane tortuosity factor.

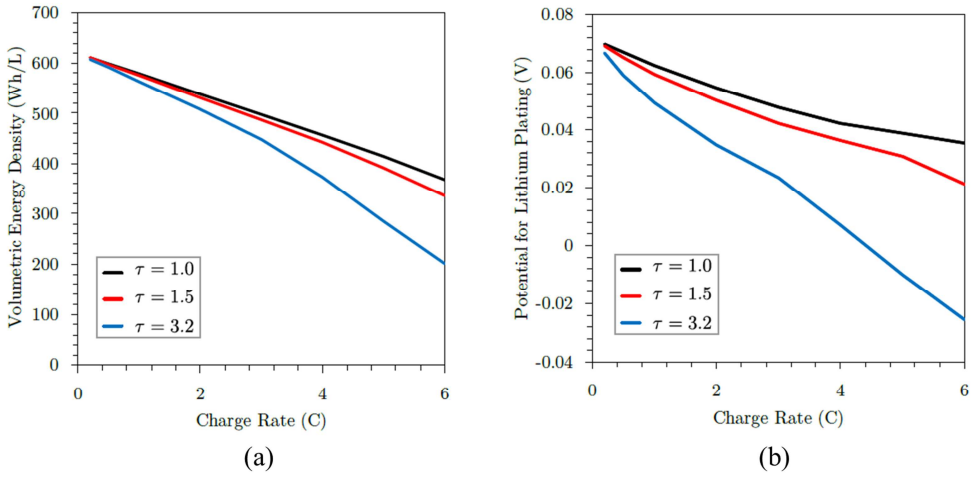

Figure 16. (a) Volumetric energy density and (b) Potential for lithium plating as a function of CC charge up to 4.2 V. The three different tortuosity factors, τ^{tp}, of 1, 1.5, and 3.2 represent: theoretical limit for all novel electrode designs, representative value achievable with an SPN, and a conventional electrode with spherical particles, respectively.

6. Discussion

The analytical model allows investigation of a large parameter space, especially evaluating the impact of parameters independently, as done in §4.2—even though through-plane tortuosity factor

coefficients α, γ and tortuosity factor anisotropy $\tau^{tp/ip}$ are not necessarily independent variables. An example of such dependence is illustrated with case 2, for which the high through-plane tortuosity factor is induced by the flake-like particle alignment [27]. Such consideration implies that the parameter space of 2D maps with α or γ for one axis and $\tau^{tp/ip}$ for the other axis, such as figures 12a and b, is not applicable in its entirety for every type of microstructure. Furthermore, the lower limit of α (1.5) corresponds to spherical particles spatially randomly distributed according to the Bruggeman analytical law, and thus to a unit $\tau^{tp/ip}$. Nevertheless, geometry examples with isotropic transport and high tortuosity factor exist as well.

The choice of the SPN is dependent on the choice of the optimization objectives. While all three objectives considered in this work are relevant because they address the fundamental trade-off issue induced by SPN architecture between improved through-plane diffusion for the structured electrode and the degraded in-plane diffusion for the primary region, they are not the unique possible choice. Especially, due to the lack of other considerations, a neutral balance has been considered: an isotropic diffusion coefficient for the second optimization objective and an isotropic characteristic diffusion time for the third optimization objective. Such an assumption, that both diffusion directions have the same weight, is debatable. For example, low width-to-thickness ratios of primary region R_t leads to recommending very high R_V values, close to their maximum $\varepsilon_{E,base}$, no matter the other parameters (cf. Table 5). This suggests the constraint $t_{tot}^{tp}/t_1^{ip} = 1$ could be relaxed, with a smaller in-plane characteristic diffusion time (i.e., $t_{tot}^{tp}/t_1^{ip} > 1$), even though the typical recommended low values for R_V of table 5 are in the range of the typical values reported in the literature (e.g., 13% [10], 22% [11], 20-25% [25]). Differences with other models' recommendation are derived from the simplified physics considered in this work and form the choice of the optimization functions.

As stated in the introduction section, such a diffusion-only approach is not enough to quantify the expected gain brought by such SPN architectures and then must be considered as a fast prescreening tool from an optimization perspective. Indeed, SPN's benefits strongly depend on the operating conditions as shown by many authors [7,8,9,13,17,22,23,24,25]. A preliminary study performed using a pseudo-2D electrochemical model (cf. §5) revealed that significant benefits can be achieved with the low tortuosity offered by an SPN. However, the standard pseudo-2D model does not account for the in-plane gradient induced by the SPN architecture geometry and considers isotropic diffusion. However, the analytical model indicated tortuosity factor anisotropy is an important parameter to decide the optimal SPN design. Therefore, to provide a more comprehensive analysis and complement this work, a 2D electrochemical COMSOL model has been developed to investigate the impact of an SPN on the electrochemical response considering different operating conditions, electrochemical parameters, and cell configuration; it is presented in Part 2 [21].

Lastly, it is worth indicating that an SPN architecture alone may not be sufficient to enable fast charging for thick electrodes, which is likely to require a combination of improvements (e.g., better electrolyte and higher temperature) as discussed in the previous work [1].

7. Conclusions

An analytical model has been developed to investigate the impact of a secondary pore network on the ionic diffusion, discriminating between the benefit on the through-plane diffusion for the whole electrode and the hindrance on the in-plane diffusion within the porous matrix. Variables of the three optimization functions considered in this work have all been analytically identified, ensuring the design optimization studies have been performed on all of the relevant parameters. The relevant SPN design parameters identified are the SPN volume fraction R_V and the width-to-thickness ratio of primary region R_t, while the relevant tortuosity factor coefficients are α and γ (from the generalized Archie's law) and the tortuosity factor anisotropy $\tau^{tp/ip}$. Also, it has provided analytical insights for the choice of the optimal design parameters, including extreme cases such as $L \gg w_1$, which are hardly investigable with numerical models. Furthermore, it has provided strong grounds for the choice of the parameter expression of the numerical electrochemical model that complements this work in Part 2 [21]. Being analytical, the model evaluation is fast, allowing a sweep of a very large design space in order to down-select promising parameter values worth investigating with more CPU expensive detailed numerical models.

The model indicates that the intrinsic limitation of an SPN lies in the exponential in-plane diffusion rate loss within the porous matrix, while the through-plane diffusion rate gain is only linear, as the first is controlled by a tortuosity-porosity power law and the second by a rule of mixture. This result explains the relatively low SPN volume fraction R_V recommended in this work, but also the values found in the literature. The maximum overall diffusion gain that maximizes through-plane gain and minimizes in-plane diffusion loss is higher for highly tortuous electrodes (high tortuosity coefficients and low porosity) and requires higher R_V to be reach compared with low tortuous electrodes. Better diffusion trade-offs are achievable for high tortuous electrodes. For very low tortuous electrode materials, there is no or limited gain to be expected from an SPN in terms of overall diffusion improvement. Significantly higher diffusion gain can be achieved if the thickness constraint is relaxed; however, the gravimetric and volumetric-specific theoretical capacity are then degraded between the baseline and structured electrodes.

Electrodes with higher total porosity can afford a larger SPNs because the penalty to densify the porous matrix is smaller for initial high porosity. Similarly, thicker electrodes can use larger SPNs because they benefit more from reducing the initially large through-plane characteristic diffusion time. For the extreme case $L \gg w_1$, the theoretical maximum $R_V = \varepsilon_{E,base}$ is recommended, which corresponds to an ultra-thick electrode with a fully dense primary region. Electrodes that combine high through-plane tortuosity factor and low in-plane tortuosity factor (i.e., high $\propto$ and/or γ and high $\tau^{tp/ip}$) particularly benefit from an SPN architecture because the model predicts both significant diffusion gain and wider choice of R_V. This especially fits well graphite with flake-like particles misaligned with the diffusing path.

Applied to a fully dense primary region, the model identified parameter spaces for which both in-plane solid-state diffusion and through-plane electrolyte diffusion are balanced. The optimal region is bounded by electrolyte transport limitation (large thickness and small primary region width region), and by solid-state transport limitation (small thickness and large primary region width region). The model

indicates that freeze-cast ultra-thick electrodes with a moderate primary region width that undergo a post-processing sintering step is an adequate combination to satisfy this criterion.

The analytical model presented in the work is available open source online [38] to the battery community and can be used to quickly prescreen tortuosity coefficients and SPN dimensions.

Acknowledgment

This work was authored in part by the National Renewable Energy Laboratory, operated by Alliance for Sustainable Energy, LLC, for the U.S. Department of Energy (DOE) under Contract No. DE-AC36-08GO28308. Funding was provided by the U.S. DOE Office of Vehicle Technology Extreme Fast Charge Cell Evaluation of Lithium-Ion Batteries (XCEL) Program, program manager Samuel Gillard. The views expressed in the article do not necessarily represent the views of the DOE or the U.S. Government. The U.S. Government retains and the publisher, by accepting the article for publication, acknowledges that the U.S. Government retains a nonexclusive, paid-up, irrevocable, worldwide license to publish or reproduce the published form of this work, or allow others to do so, for U.S. Government purposes.

Appendices

Appendix A: Design Recommendation Expressed with R_w

The model is insensitive to the channel geometry presented in figure 3 under the condition that the SPN volume ratio R_V is used as the design parameter. This is derived from the rule of mixture used to deduce the structured electrode through-plane diffusion coefficient that considers region volume as weights (cf. eq. 6a). Because of this, a metric not based on region volume (e.g., the secondary-region-width to primary-region-width ratio, R_w, cf. eq. 19) introduces a model dependence with the channel geometry because a bijection exists between this nonvolume-based metric and the channel geometry with R_V.

This is illustrated in figure A.1–A.3, for which the primary region porosity (cf. Fig. A.1), the diffusion gain product (cf. Fig. A.2), and the optimal R_w according to the third optimization objective (cf. Fig. A.3) are plotted for case 1 (cf. Table 4) for both rectangular and cylindrical channels considering R_w as the SPN design parameter. Design recommendation R_w differs significantly between the two channel geometries. For example, for $\varepsilon_{E,base}$=0.3 and R_t=1, the optimal R_w is 0.19 and 0.83, respectively, for rectangular and cylindrical channels (cf. Fig. A.3). In both cases, this corresponds to a diffusion gain product of 0.75 (cf. Fig. A.2), which is the same gain obtained considering R_V (cf. Table 5). This difference comes from a different width ratio is required to obtain the same volume ratio between the two-channel geometry (cf. eq. 4a, 4b).

While results are more generic with R_V, presenting them with the region width ratio instead is also relevant at the condition the channel geometry considered is indicated. Readers can regenerate figures of this article with R_w as a design parameter using the open-source model developed for this work available there [38].

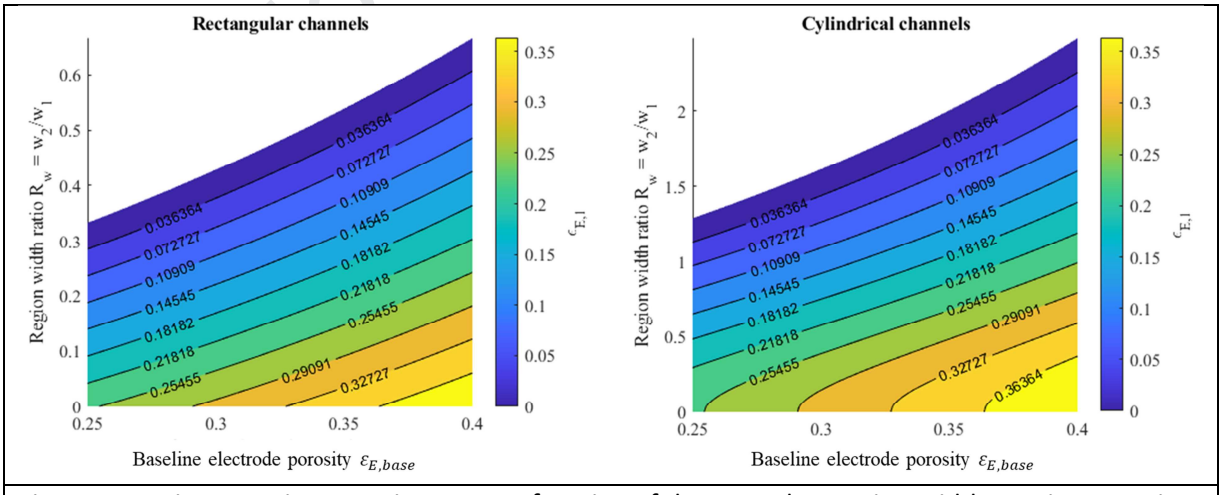

Figure A.1. Primary region porosity $\varepsilon_{E,1}$ as a function of the secondary region-width to primary region-width ratio R_w and of the baseline electrode porosity $\varepsilon_{E,base}$. Empty map space corresponds to impossible design space (negative porosity). (Left) Channels are rectangular, (right) channels are cylindrical, as described in figure 3.

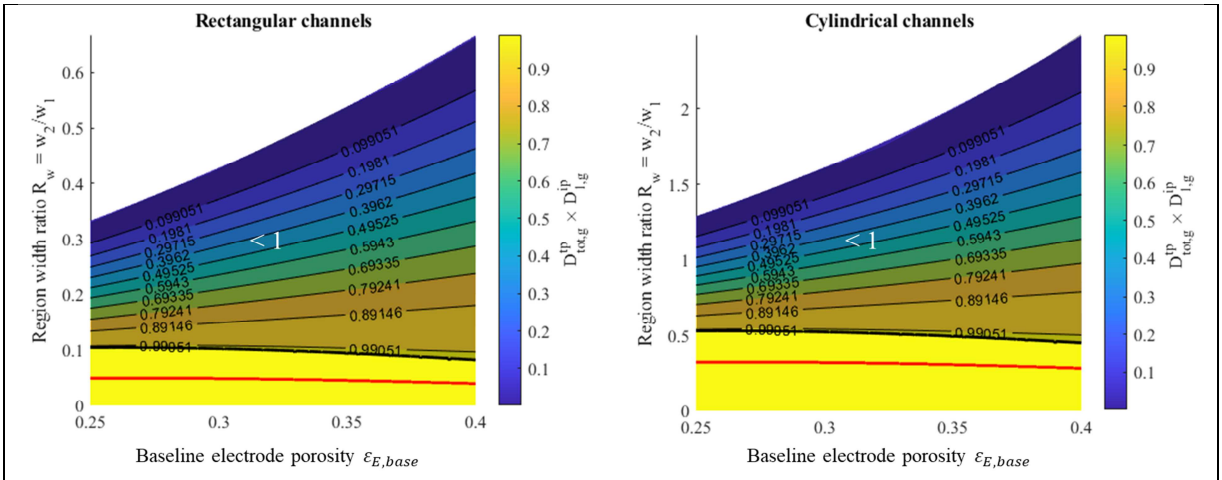

Figure A.2. Diffusion gain product map as a function of baseline electrode porosity $\varepsilon_{E,base}$ and the secondary region-width to primary region-width ratio R_w for case 1. (Left) Channels are rectangular, (right) channels are cylindrical. Unit isoline is the black line and optimal R_V that maximizes diffusion gain product is the red line (first optimization objective). The transparent grey area corresponds to a diffusion gain product below 1; thus, an overall loss region to avoid.

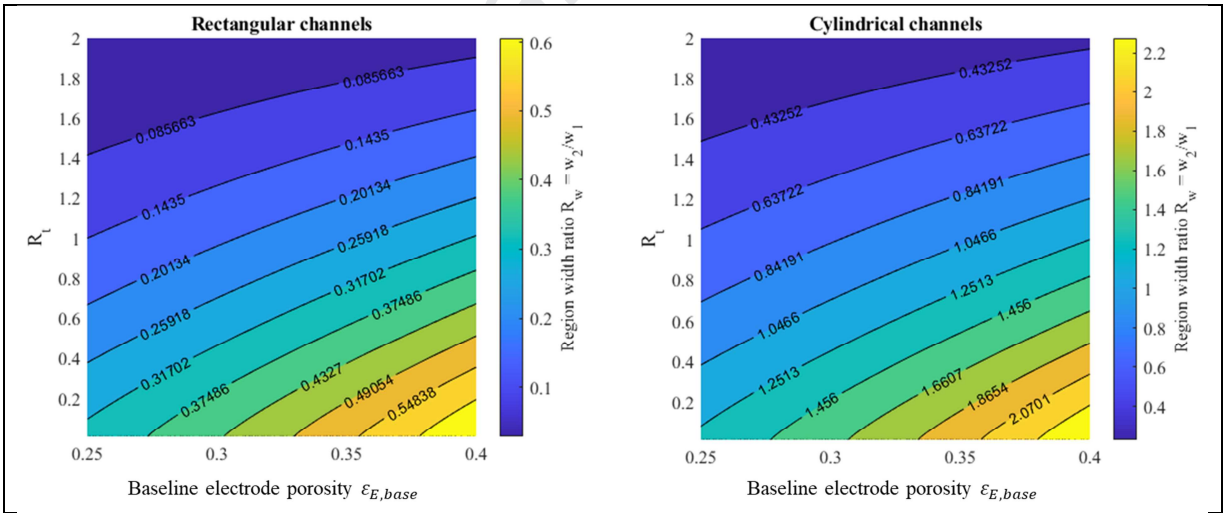

Figure A.3. Optimal secondary region-width to primary region-width ratio R_w considering third optimization objective, enforce isotropic characteristic diffusion time, with 2D map being the optimal values for case 1. (Left) Channels are rectangular, (right) channels are cylindrical.

Appendix B: Considering Identical Porosity between Primary Region and Baseline Electrodes

In this case, baseline electrode and primary region of the structured electrode share the same porosity: $\varepsilon_{E,1} = \varepsilon_{E,base}$ then $L > L_{base}$. This comparison approach is relevant when there is not a strict

constraint on the gravimetric and volumetric-specific theoretical capacity. Figure B.1 shows the normalized thickness of the structured electrode within the range of the investigated baseline electrode porosity. To keep the active material mass identical to the baseline electrode, increasing the SPN volume ratio or the region-width ratio requires an increase to the structured electrode thickness. For example, a 20% SPN volume fraction induces a 25% increase of the electrode thickness (cf. Fig. B.1).

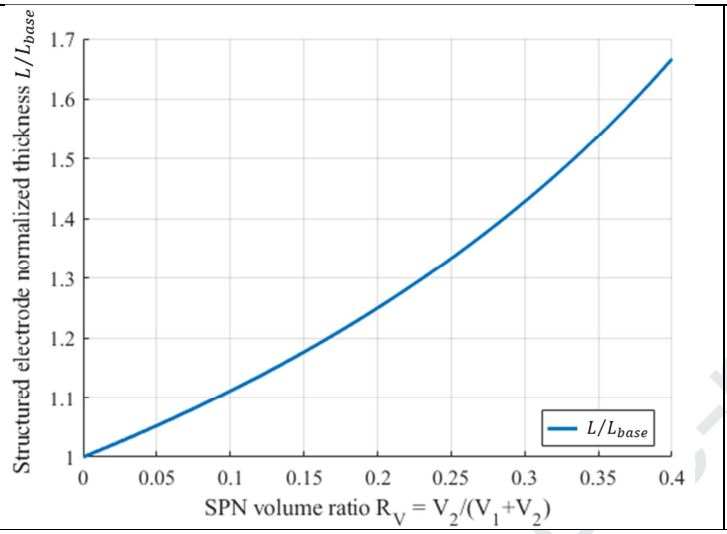

Figure B.1. Structured electrode thickness L normalized with baseline electrode thickness L_{base} as a function of the secondary pore network volume fraction R_V for cases 4 and 5.

Because the primary region porosity $\varepsilon_{E,1}$is kept identical with the baseline electrode porosity $\varepsilon_{E,base}$, the SPN does not induce ionic in-plane transport degradation (i.e., $D_{1,g}^{ip} = 1$). Therefore, a significantly higher diffusion product gain can be achieved compared with the previous constant thickness case discussed in §4.1. For example, at $\varepsilon_{E,base} = 0.3$ and $R_V = 0.2$, cases 4 and 5 (identical porosity), exhibit an overall diffusion gain of, respectively, 3.01 and 5.01 (cf. Fig. B.2), while cases 1 and 2 (identical thickness) only reach 0.54 and 0.76 (cf. Fig. 8); thus, a 5.5 to 6.5 times increase. Cases 1,4 and 2,5 share the same tortuosity coefficients and are then comparable.

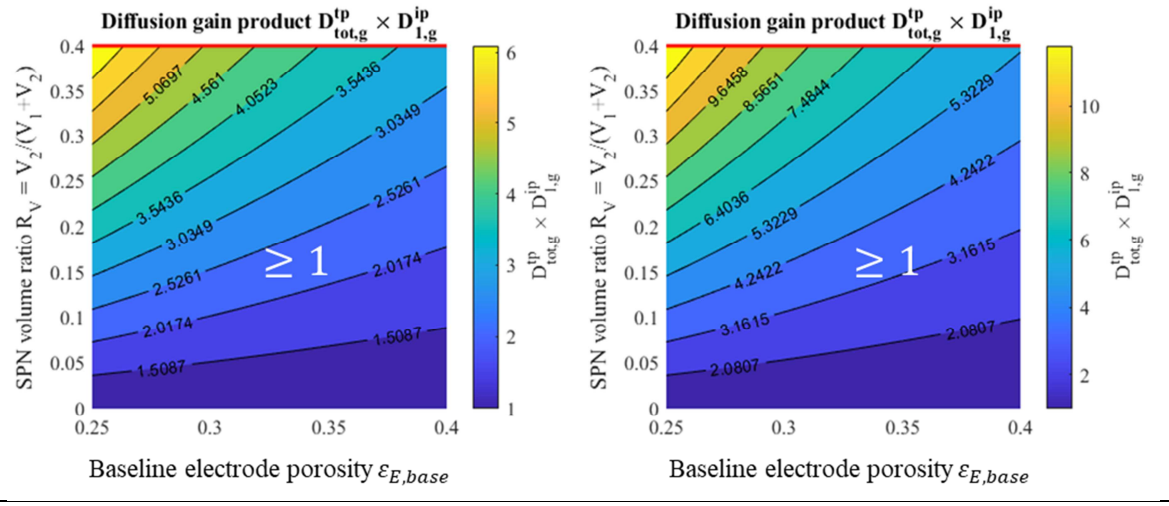

Figure B.2. Diffusion gain product map as a function of baseline electrode porosity $\varepsilon_{E,base}$ and the SPN volume fraction R_V for (left) case 4 and (right) case 5 electrodes. Because the primary region in-plane diffusion gain $D_{1,g}^{ip}$ is equal to 1, no optimal value of R_V can be determined: the maximum gain product corresponding to the maximum R_V (red line).

Lower R_V are recommended to achieve the diffusion coefficient isotropy (cf. Fig. B.3, top) compared with first optimization objectives. Although, compared to cases 1 and 2 (constant thickness, cf. Fig. 9, left column), higher values are recommended, cf. Table B.1. For the optimal SPN, a higher diffusion gain is achieved relaxing the thickness constraint. For moderately low width-to-thickness ratio of primary region R_t, there is no solution to achieve isotropic diffusion time (cf. Fig. B.3, bottom). Indeed, t_1^{ip} is constant while t_{tot}^{tp} is continuously increasing with the thickness once $R_V \to 1$. This domain restriction is derived from our neutral definition of the optimization objective (balancing in-plane and through-plane diffusion time without favoring one direction). This region still corresponds to a significant overall diffusion gain as shown in figure B.2.

Table B.1. Design parameter recommendation.[1]Optimal SPN volume fraction R_V deduced from third optimization objective. Diffusion product gain $D_{tot,g}^{tp} \times D_{1,g}^{ip}$ values are provided for this optimal R_V.

$\varepsilon_{E,base}$	Comparison	Low tortuosity, low anisotropy (case 1,4)		High tortuosity, high anisotropy, (case 2,5)	
		Optimal[1] R_V	$D_{tot,g}^{tp} \times D_{1,g}^{ip}$	Optimal[1] R_V	$D_{tot,g}^{tp} \times D_{1,g}^{ip}$
0.3	Identical thickness (case 1,2)	16.3%	0.75	14.9%	1.22
	Variable thickness (case 4,5)	47.5%	5.74	43.9%	9.89
0.4	Identical thickness (case 1,2)	24.4%	0.61	23.0%	0.91
	Variable thickness (case 4,5)	83.3%	5.77	81.0%	9.92

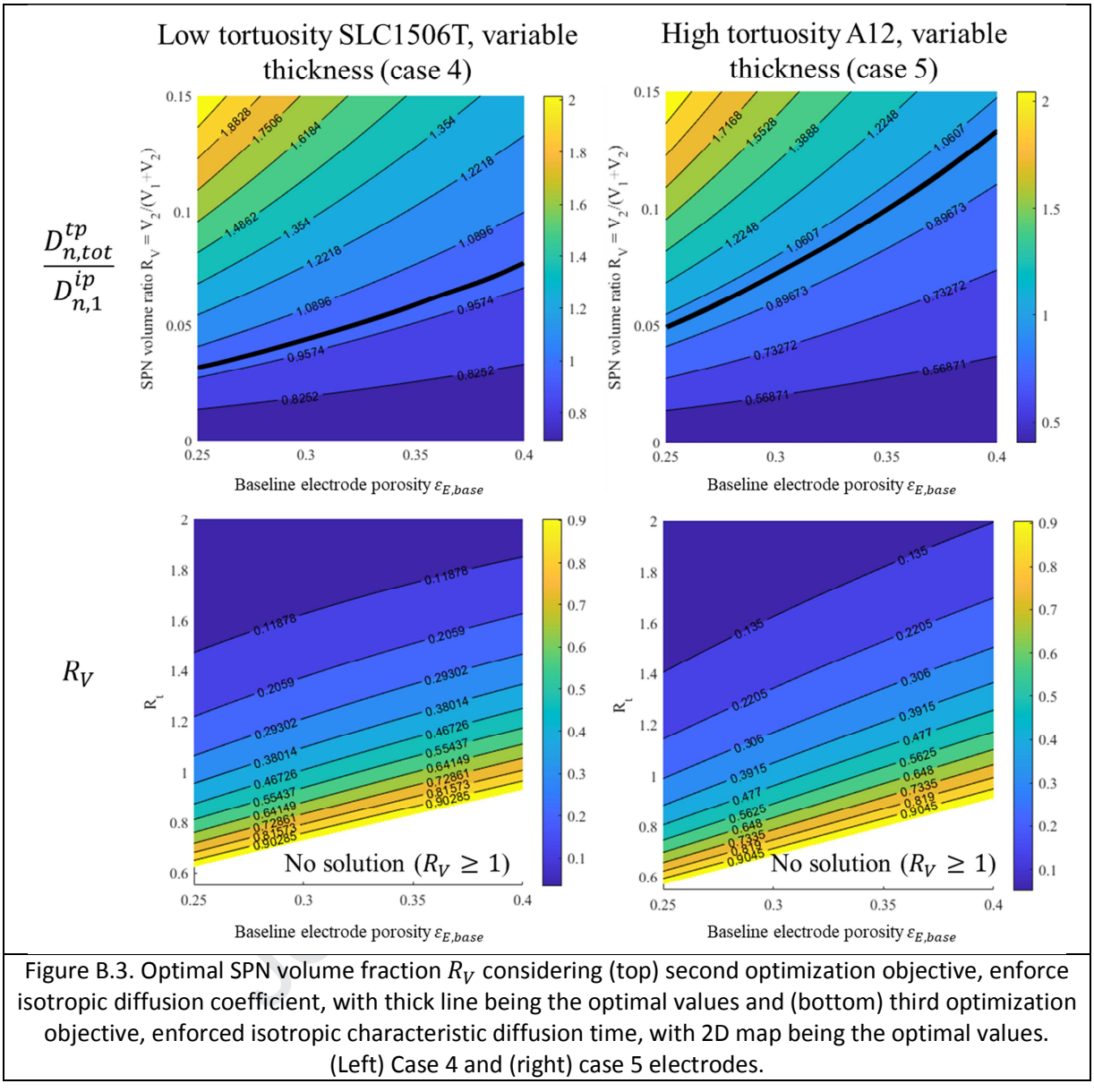

Figure B.3. Optimal SPN volume fraction R_V considering (top) second optimization objective, enforce isotropic diffusion coefficient, with thick line being the optimal values and (bottom) third optimization objective, enforced isotropic characteristic diffusion time, with 2D map being the optimal values. (Left) Case 4 and (right) case 5 electrodes.

Appendix C: Bilayer Study

Bilayer cases 12 and 13 are presented in this appendix. Both use the same parameters of case 1 (low through-plane tortuosity coefficients, low tortuosity anisotropy), but with R_L = 0.9 and 0.8, respectively. The term R_L refers to the primary region-thickness ratio as defined in eq. 21 and is illustrated in figure 2. Because of the additional pad at the back of the electrode, the densification of the primary (and third) region is less pronounced with R_V because R_L decreases (cf. Fig. C.1). The definition of R_V is unchanged (cf. eq. 14) and does not include the third region volume V_3.

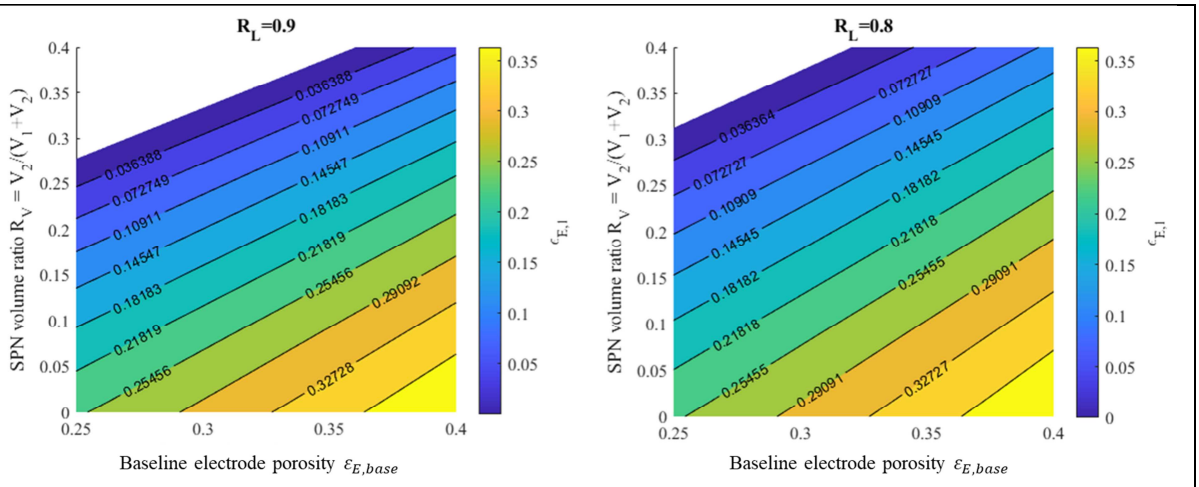

Figure C.1. Primary region porosity $\varepsilon_{E,1}$ as a function of the secondary region volume fraction R_V and of the baseline electrode porosity $\varepsilon_{E,base}$. Empty map space corresponds to impossible design space (negative porosity). Note that R_V can exceed $\varepsilon_{E,base}$ because of the presence of the third region. (Left) Case 12, and (right) case 13.

Bilayer architecture offers two different, nonequivalent, approaches to calculate the effective through-plane diffusion coefficient as discussed in §3.1.2. Therefore, the model only provides bounds. Figure C.2 shows the normalized through-plane diffusion coefficient of the structured electrode, using a parallel then series approach, $D_{n,tot}^{tp*}$, (cf. eq. 6b) and using a series then parallel approach, $D_{n,tot}^{tp**}$, (cf. eq. 6c). The first approach provides the upper bound while the second approach provides the lower bound (cf. Fig. C.2). If the electrolyte concentration would be roughly similar between the primary and secondary regions (i.e., in-plane concentration gradient negligible), then it would be more relevant to homogenize these two regions first (i.e., using the parallel then series approach). Although, such considerations would require a 2D electrochemical model to eventually choose between the two approaches. Unlike the unilayer case for which $D_{n,tot}^{tp}$ is monolithically increasing with R_V (cf. Fig. 6b), the normalized through-plane diffusion coefficient of the structured electrode reaches a maximum then decreases with R_V (cf. Fig. C.2). This is because the densification of the third region with R_V will eventually block the through-plane diffusion. The diffusion trade-off problem is thus more complex compared with the unilayer case for which SPN was always improving the through-plane diffusion and degrading the primary region in-plane diffusion. Therefore, for the same R_V and $\varepsilon_{E,base}$: $D_{n,tot}^{tp} > D_{n,tot}^{tp*} > D_{n,tot}^{tp**}$ with difference increasing for lower values of R_L. As a result, the diffusion gain product is also lower compared with the unilayer case and follows the same hierarchy (cf. Fig. C.3).

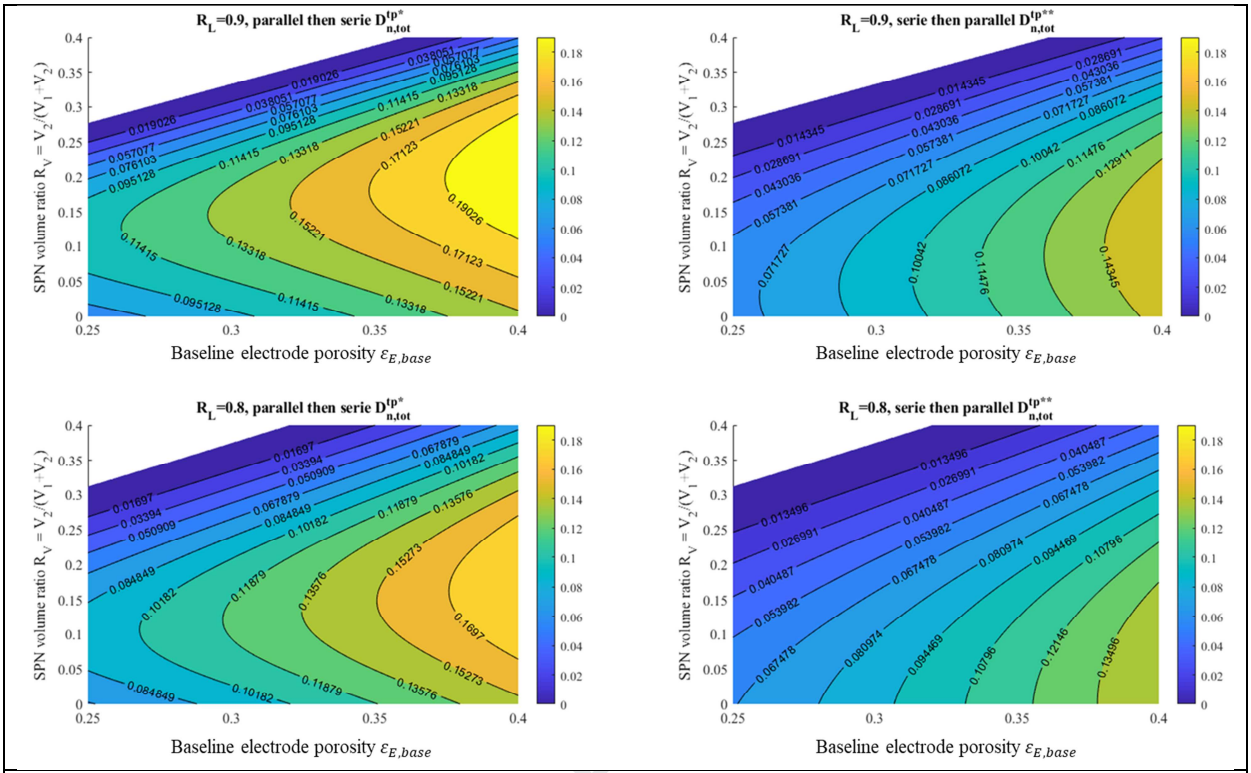

Figure C.2. Normalized through-plane diffusion coefficient of structured electrode using (left) a parallel then series approach $D_{n,tot}^{tp*}$ and (right) a series then parallel approach $D_{n,tot}^{tp**}$. (Top) Case 12 and (bottom) case 13.

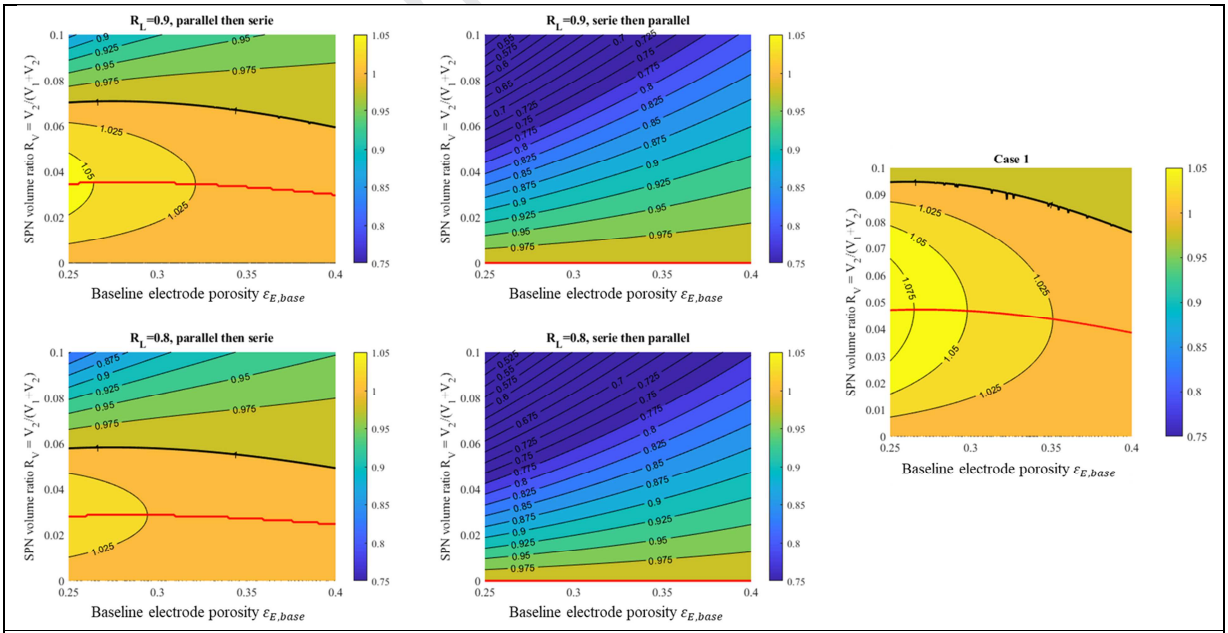

Figure C.3. Diffusion gain product map as a function of baseline electrode porosity $\varepsilon_{E,base}$ and the SPN volume fraction R_V electrode using (left) a parallel then series approach and (middle) a series then parallel approach for (top) case 12 and (bottom) case 13. (right) Case 1 unilayer is shown for

comparison. Unit isoline is the black line, and optimal R_V that maximizes diffusion gain product is the red line (first optimization objective).

Because the in-plane diffusion penalty is lower for the bimodal case, because the primary region densification is lower at the same R_V, and both in-plane and through-plane diffusion suffers from large R_V, higher R_V are required to achieve isotropic diffusion time (cf. Fig. C.4). For infinitely low width-to-thickness ratio of the primary region, no solution exists because the through-plane diffusion time is excessively high due to the third region thickness being magnitudes larger than the primary region width.

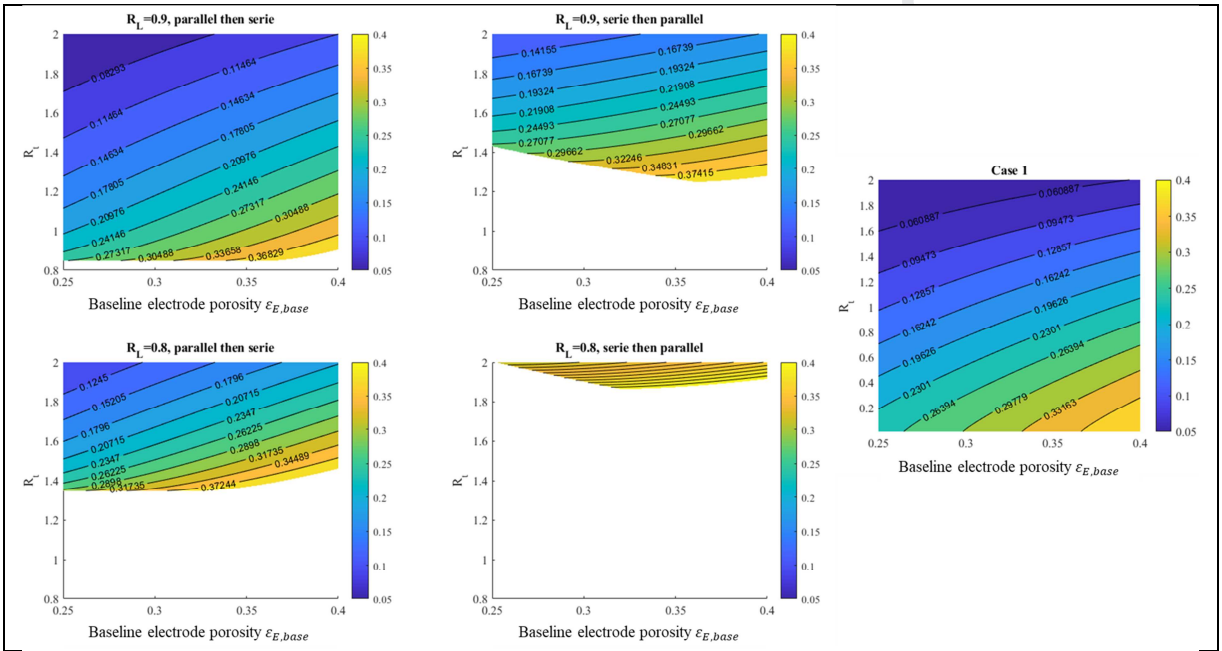

Figure C.4. Optimal SPN volume fraction R_V considering third optimization objective, enforce isotropic characteristic diffusion time with 2D map being the optimal values, using (left) a parallel then series approach and (middle) a series then parallel approach for (top) case 12 and (bottom) case 13. (Right) Case 1 unilayer is shown for comparison. Empty space corresponds to negative porosity.

References

[1] A. M. Colclasure, A. R. Dunlop, S. E. Trask, B. J. Polzin, A. N. Jansen, and K. Smith, Requirements for Enabling Extreme Fast Charging of High Energy Density Li-Ion Cells while Avoiding Lithium Plating, Journal of the Electrochemical Society, 166(8) (2019) A1412, DOI: 10.1149/2.0451908jes.

[2] S. Ahmed, I. Bloom, A. N. Jansen, T. Tanim, E. J. Dufek, A. Pesaran, A. Burnham, R. B. Carlson, F. Dias, and K. Hardy, Enabling fast charging - A battery technology gap assessment, Journal of Power Sources, 367 (2017), 250, http://dx.doi.org/10.1016/j.jpowsour.2017.06.055

[3] M. Keyser, A. Pesaran, Q. Li, S. Santhanagopalan, K. Smith, E. Wood, S. Ahmed, I. Bloom, E. Dufek, and M. Shirk, Enabling fast charging - Battery thermal considerations, Journal of Power Sources, 367 (2017) 228, http://dx.doi.org/10.1016/j.jpowsour.2017.07.009.

[4] A. M. Colclasure, T. R. Tanim, A. N. Jansen, S. E. Trask, A. R. Dunlop, B. J. Polzin, I. Bloom, D. Robertson, L. Flores, M. Evans, E. J. Dufek, and K. Smith, Electrode scale and electrolyte transport effects on extreme fast charging of lithium-ion cells, Electrochimica Acta, 337 (2020) 135854, https://doi.org/10.1016/j.electacta.2020.135854

[5] G. E. Archie, Dallas Meeting (1941)

[6] I. V. Thorat, D. E. Stephenson, N. A. Zacharias, K. Zaghib, J. N. Harb, and D. R. Wheeler, Quantifying tortuosity in porous Li-ion battery materials, Journal of Power Sources, 188 (2009) 592, https://doi.org/10.1016/j.jpowsour.2008.12.032

[7] J. S. Sander, R. M. Erb, L. Li, A. Gurijala, and Y.-M. Chiang, High-performance battery electrodes via magnetic templating, Nature Energy, 1 (2016) 16099, https://doi.org/10.1038/nenergy.2016.99.

[8] C.-J. Bae, C. K. Erdonmez, J. W. Halloran, and Y.-M. Chiang, Design of Battery Electrodes with Dual-Scale Porosity to Minimize Tortuosity and Maximize Performance, Advanced Materials, 25 (2013) 1254, https://doi.org/10.1002/adma.201204055.

[9] J.-H. Rakebrandt, P. Smyrek, Y. Zheng, H.J. Seifert, and W. Pfleging, Laser processing of thick Li(NiMnCo) O2 electrodes for lithium-ion batteries, Proceedings of SPIE, 10092 (2017) 100920M, doi: 10.1117/12.2252093.

[10] J. Park, S. Hyeon, S. Jeonga, and H.-J. Kim, Performance enhancement of Li-ion battery by laser structuring of thick electrode with low porosity, Journal of Industrial and Engineering Chemistry, 70 (2019) 178, https://doi.org/10.1016/j.jiec.2018.10.012.

[11] J. B. Habedank, L. Kraft, A. Rheinfeld, C. Krezdorn, A. Jossen, and M. F. Zaeh, Increasing the Discharge Rate Capability of Lithium-Ion Cells with Laser-Structured Graphite Anodes: Modeling and Simulation, Journal of the Electrochemical Society, 165(7) (2018), A1563, DOI: 10.1149/2.1181807jes.

[12] S. Behr, R. Amin, Y.-M. Chiang, and A. P. Tomsia, Highly-Structured, Additive-Free Lithium-Ion Cathodes by Freeze-Casting Technology, CFI Ceramic Forum International, 92(4) (2015) E39.

[13] B. Delattre, R. Amin, J. Sander, J. D. Coninck, A. P. Tomsia, and Y.-M. Chiang, Impact of Pore Tortuosity on Electrode Kinetics in Lithium Battery Electrodes: Study in Directionally Freeze-Cast LiNi0.8Co0.15Al0.05 O2 (NCA) , Journal of Electrochemical Society, 165(2) (2018) A388, DOI: 10.1149/2.1321802jes.

[14] C. Huang and P. S. Grant, Coral-like directional porosity lithium ion battery cathodes by ice templating, Journal of Materials Chemistry A, 6 (2018) 14689, DOI: 10.1039/c8ta05049j.

[15] R. Amin, B. Delattre, A. P. Tomsia, and Y.-M. Chianh, Electrochemical Characterization of High Energy Density Graphite Electrodes Made by Freeze-Casting, ACS Applied Energy Materials, 1(9) (2018) 4976, DOI: 10.1021/acsaem.8b00962.

[16] S. W. Sofie, Fabrication of Functionally Graded and Aligned Porosity in Thin Ceramic Substrates With the Novel Freeze–Tape-Casting Process, Journal of American Ceramic Society, 90(7) (2007) 2024, DOI: 10.1111/j.1551-2916.2007.01720.x.

[17] M. A. Ghadkolai, S. Creager, J. Nanda, R. K. Bordia, Freeze Tape Cast Thick Mo Doped Li4Ti5O12 Electrodes for Lithium-Ion Batteries, Journal of the Electrochemical Society,164(12) (2017) A2603, DOI: 10.1149/2.1311712jes.

[18] Y. Hwa, E. Yi, H. Shen, Y. Sung, J. Kou, K. Chen, D. Y. Parkinson, M. M. Doeff, E. J. Cairns, Three-Dimensionally Aligned Sulfur Electrodes by Directional Freeze Tape Casting, Nano Letters, 19 (2019) 4731, DOI: 10.1021/acs.nanolett.9b01805.

[19] E. R. Reale, and K. C. Smith, Capacitive Performance and Tortuosity of Activated Carbon Electrodes with Macroscopic Pores, Journal of Electrochemical Society, 165(9) (2018) A1685, http://dx.doi.org/10.1149/2.0601809jes

[20] A. P. Bhat, E. R. Reale, M. del Cerro, K. C. Smith, and R. D. Cusick, Reducing impedance to ionic flux in capacitive deionization with Bi-tortuous activated carbon electrodes coated with asymmetrically charged polyelectrolytes, Water Research X, 3(1) (2019) 100027, https://doi.org/10.1016/j.wroa.2019.100027

[21] W. Mai, F. Usseglio-Viretta, A. Colclasure, K. Smith, Enabling Fast Charging of Lithium-Ion Batteries through Secondary-/Dual- Pore Network: Part II - numerical model, Electrochimica Acta, (2019), submitted.

[22] J. Billaud, F. Bouville, T. Magrini, C. Villevieille, and A. R. Studart, Magnetically aligned graphite electrodes for high-rate performance Li-ion batteries, Nature Energy,1 (2016) 16097, DOI: 10.1038/NENERGY.2016.97.

[23] C. L. Cobb and M. Blanco, Modeling mass and density distribution effects on the performance of co-extruded electrodes for high energy density lithium-ion batteries, Journal of Power Sources, 249(1) (2014) 357, http://dx.doi.org/10.1016/j.jpowsour.2013.10.084.

[24] C. L. Cobb and S. E. Solberg, Communication—Analysis of Thick Co-Extruded Cathodes for Higher-Energy-and-Power Lithium-Ion Batteries, Journal of the Electrochemical Society, 164(7) (2017) A1339, DOI: 10.1149/2.0101707jes.

[25] V. P. Nemani, S. J. Harris, and K. C. Smith, Design of Bi-Tortuous, Anisotropic Graphite Anodes for Fast Ion-Transport in Li-Ion Batteries, Journal of the Electrochemical Society, 162(8) (2015) A1415, DOI: 10.1149/2.0151508jes.

[26] M. Ebner, D.-W. Chung, R. E. Garcia, and V. Wood, Tortuosity Anisotropy in Lithium-Ion Battery Electrodes, Advanced Energy Materials, 4 (2014) 1301278, DOI: 10.1002/aenm.201301278.

[27] F. L. E. Usseglio-Viretta, A. Colclasure, A. N. Mistry, K. P. Y. Claver, F. Pouraghajan, D. P. Finegan, T. M. M. Heenan, D. Abraham, P. P. Mukherjee, D. Wheeler, P. Shearing, S. J. Cooper, and K. Smith, Resolving the Discrepancy in Tortuosity Factor Estimation for Li-Ion Battery Electrodes through Micro-Macro Modeling and Experiment, Journal of the Electrochemical Society, 165(14) (2018) A3403, DOI: 10.1149/2.0731814jes.

[28] B. Delattre, H. Bai, R. O. Ritchie, J. D. Coninck, and A. P. Tomsia, Unidirectional Freezing of Ceramic Suspensions: In Situ X□ray Investigation of the Effects of Additives, ACS Applied Materials and Interfaces, 6(1) (2014) 159, dx.doi.org/10.1021/am403793x.

[29] M. M. Porter, R. Imperio, M. Wen, M. A. Meyers, and J. McKittrick, Bioinspired Scaffolds with Varying Pore Architectures and Mechanical Properties, Advanced Functional Materials, 24 (2014) 1978, DOI: 10.1002/adfm.201302958.

[30] I. Nelson, S. E. Naleway, Intrinsic and extrinsic control of freeze casting, Journal of Materials Researche and Technology, 8(2) (2019) 23712, https://doi.org/10.1016/j.jmrt.2018.11.011.

[31] Y. Zhang, W. Luo, C. Wang, Y. Li, C. Chen, J. Song, J. Dai, E. M. Hitz, S. Xu, C. Yang, Y. Wang Y, and L. Hu, High-capacity, low-tortuosity, and channel-guided lithium metal anode, Proceedings of the National Academy of Sciences of the United States of America, 114(14) (2017) 3584, https://doi.org/10.1073/pnas.1618871114.

[32] H. Iwai, A. Kuroyanagi, M. Saito, A. Konno, H. Yoshida, T. Yamada, and S. Nishiwaki, Power generation enhancement of solid oxide fuel cell by cathode–electrolyte interface modification in mesoscale assisted by level set-based optimization calculation, Journal of Power Sources, 196(7) (2011) 3485, doi:10.1016/j.jpowsour.2010.12.024.

[33] D. Roussel, A. Lichtner, D. Jauffrès, J. Villanova, R. K. Bordia, C. L. Martin, Strength of hierarchically porous ceramics: Discrete simulations on X-ray nanotomography images, Scripta Materialia, 113(1) (2016) 250, http://dx.doi.org/10.1016/j.scriptamat.2015.11.015.

[34] J. Villanova, P. Cloetens, H. Suhonen, J. Laurencin, F. Usseglio-Viretta, E. Lay, G. Delette, P. Bleuet, D. Jauffrès, D. Roussel, A. Z. Lichtner, and C. L. Martin, Multi-scale 3D imaging of absorbing porous materials for solid oxide fuel cells, Journal of Materials Science, 49 (2014) 5626, DOI 10.1007/s10853-014-8275-3.

[35] C. Gaudillere, J. M. Serra, Freeze-casting: Fabrication of highly porous and hierarchical ceramic supports for energy applications, boletín de la sociedad española de cerámica y vidrio, 55 (2016) 45, https://doi.org/10.1016/j.bsecv.2016.02.002.

[36] R. Liu, T. Xu, C-A. Wang, A review of fabrication strategies and applications of porous ceramics prepared by freeze-casting method, Ceramics International, 42(2) (2016) 2907, https://doi.org/10.1016/j.ceramint.2015.10.148.

[37] K. L. Scotti, D. C. Dunand, Freeze casting – A review of processing, microstructure and properties via the open data repository, FreezeCasting.net, Progress in Materials Science, 94 (2018) 243, https://doi.org/10.1016/j.pmatsci.2018.01.001.

[38] Secondary pore network design optimization analytical diffusion model for lithium ion battery, https://www.nrel.gov/transportation/electrode_secondaryporenetwork.html

[39] J. Wang, J. K. Carson, M. F. North, D. J. Cleland, A new approach to modelling the effective thermal conductivity of heterogeneous materials, International Journal of Heat and Mass Transfer, 49 (2006) 3075, doi:10.1016/j.ijheatmasstransfer.2006.02.007.

[40] G.-H. Kim, K. Smith, J. Lawrence-Simon, and C. Yang, Efficient and Extensible Quasi-Explicit Modular Nonlinear Multiscale Battery Model: GH-MSMD, Journal of the Electrochemical Society, 164(6) (2016) A1076, DOI: 10.1149/2.0571706jes.

Highlights

- In-plane diffusion limitation intrinsically restricts the SPN volume fraction
- High tortuosity electrodes benefit the most from SPN
- Electrodes with high tortuosity anisotropy fits well with SPN

Enabling Fast Charging of Lithium-Ion Batteries through Secondary- /Dual- Pore Network: Part I - Analytical Diffusion Model

F. L. E. Usseglio-Viretta[1], W. Mai[1], A. M. Colclasure[1], M. Doeff[2], Eongyu Yi[2], and K. Smith[1]

[1] Center for Integrated Mobility Sciences, National Renewable Energy Laboratory, Golden, CO 80401 USA

[2] Energy Storage and Distributed Resources Division, Lawrence Berkeley National Laboratory, Berkeley, CA 94720 USA

Corresponding author: A. Colclasure. Email address: Andrew.Colclasure@nrel.gov

Author Contribution Statement

F. L. E. Usseglio-Viretta: Methodology, Software, Writing - Original Draft

W. Mai: Writing - Review & Editing, Methodology

A. M. Colclasure: Writing - Review & Editing, Supervision

M. Doeff: Resources, Writing - Review & Editing

Eongyu Yi: Resources

K. Smith: Supervision, Project administration, Funding acquisition

Declaration of interests

☒ The authors declare that they have no known competing financial interests or personal relationships that could have appeared to influence the work reported in this paper.

☐The authors declare the following financial interests/personal relationships which may be considered as potential competing interests: